Journal of Alloys and Compounds 822 (2020) 153470

Contents lists available at ScienceDirect

Journal of Alloys and Compounds

journal homepage: http://www.elsevier.com/locate/jalcom

Investigation of structural, magnetic and dielectric properties of gallium substituted Z-type $Sr_3Co_{2-x}Ga_xFe_{24}O_{41}$ hexaferrites for microwave absorbers

Preksha N. Dhruv [a], Sher Singh Meena [b, **], Robert C. Pullar [c], Francisco E. Carvalho [d, e], Rajshree B. Jotania [a, *], Pramod Bhatt [b], C.L. Prajapat [f, g], João Paulo Barros Machado [h], T.V. Chandrasekhar Rao [f, g], C.B. Basak [g, i]

[a] Department of Physics, Electronics and Space Science, University School of Sciences, Gujarat University, Ahmedabad, 380 009, India
[b] Solid State Physics Division, Bhabha Atomic Research Centre, Mumbai, 400 085, India
[c] Department of Engineering of Materials and Ceramics/CICECO - Aveiro Institute of Materials, University of Aveiro, Aveiro, 3810-193, Portugal
[d] Instituto Tecnologico de Aeronautica, Praça Mal. Eduardo Gomes, 50, São José dos Campos 12.228-900, Brazil
[e] Instituto de Estudos Avançados, Trevo Cel. Av. Jose A. A. Amarante, São José dos Campos 12.228-001, Brazil
[f] Technical Physics Division, Bhabha Atomic Research Centre, Mumbai, 400 085, India
[g] Homi Bhabha National Institute, Anushaktinagar, Mumbai, 400 094, India
[h] National Institute for Space Research, Associated Laboratory for Sensors and Materials, Av. dos Astronautas, 1.758 - Jardim da Granja, São José dos Campos - SP, 12227-010, Brazil
[i] Mechanical Metallurgy Division, Bhabha Atomic Research Centre, Mumbai, 400 085, India

ARTICLE INFO

Article history:
Received 25 June 2019
Received in revised form
14 December 2019
Accepted 19 December 2019
Available online 28 December 2019

Keywords:
Gallium substituted Z-type hexaferrites
Sol-gel auto-combustion
Structural properties
Magnetic properties
Microwave absorption performance

ABSTRACT

Gallium substituted Z-type hexagonal ferrites with chemical composition $Sr_3Co_{2-x}Ga_xFe_{24}O_{41}$ ($x = 0.0, 0.4, 0.8, 1.2, 1.6$, and 2.0) were successfully synthesised in air at 1200 °C for 5 h using the sol-gel auto-combustion technique, in order to investigate the effect of gallium substitution on structural, magnetic and dielectric properties. X-ray Diffraction (XRD) analysis of all samples reveals the formation of mixed hexaferrite phases, with Z ferrite as the major phase (72–90%).The average crystallite size of heated powders was found to be in the range of 21–40 nm. The saturation magnetisation decreases after gallium substitution, with the lowest values of 64 $Am^2\ kg^{-1}$ for composition $x = 1.6$, which also hasthe highest value of coercivity (28.3 kA m^{-1}). Nevertheless, all were soft ferrites, with H_c between 3.4 and 28.3 kA m^{-1}.The M_r/M_S ratio of all samples was found to be less than 0.5, suggesting that all the compositions possess multi-domain microstructures. Mössbauer spectroscopic analysis confirmed that the Fe ions were found in the 3 + high spin state for compositions below $x \leq 0.4$, whereas ~1.5% of the Fe ions were converted into Fe^{2+} high spin state beyond $x \geq 0.8$ compositions, as Ga^{3+} began to substitute for Fe^{3+}, forming Fe^{2+} in the cobalt positions. The average hyperfine magnetic field ($<H_{hf}>$) was found to be decreased with Ga-substitution. Dielectric parameters such as dielectric constant and loss factor were studied as a function of frequency, and their results show normal behaviour for ferrimagnetic materials. In complex measurements at microwave frequencies (8 GHz–12.5 GHz, the X-band), all samples had a real permittivity of around 8–14. For sample $x = 2.0$, a dielectric resonance peak was observed around 12.15 GHz. All showed a real permeability of around 1.0–1.4 over the frequency of 8 GHz–12.5 GHz range, and ferromagnetic resonance (FMR) was observed in $x = 0.0$ and 2.0 samples, at around 11 and 12 GHz, respectively. This suggests that the prepared samples can be used as microwave absorbers/EMI shielding at specific microwave frequencies. The co-existence of FMR and dielectric resonance at the same frequency of 12.15 GHz for $x = 2.0$ could lead to the coupling of these resonances and the development of potential metamaterials.

* Corresponding author.
** Corresponding author.
E-mail addresses: ssingh@barc.gov.in (S.S. Meena), rbjotania@gmail.com (R.B. Jotania).

https://doi.org/10.1016/j.jallcom.2019.153470
0925-8388/

1. Introduction

Hexaferrites are a class of ceramic magnets having vast technological applications such as permanent magnets, nano-electromagnetic devices, microwave devices and magnetic recording media [1]. They have also gained great attention in recent years due to the development of radar absorbing materials (RAM), anti-electromagnetic and microwave shielding, interference coatings, etc. [2–4]. The excellent magnetic and dielectric properties make hexaferrites suitable magnetic materials for electromagnetic wave absorbers [5]. Recently, there has been an increasing demand on the electronic equipment such as mobile phones, laptop computers, and tablets, modems and antennas, which requires the shift to centimeter-scale wavelengths in the microwave range (3–30 GHz), and even up towards the millimeter range corresponding to >30 GHz frequencies for 5G and 6G devices. The growth of devices functioning at this GHz frequency range creates a serious risk of electromagnetic interference (EMI) problems. EMI occurs when EM signals are transmitted from unwanted sources and interfere with other electronic devices functioning within similar frequency ranges. Furthermore, health concern issues being are raised all over the world due to electromagnetic radiation, which could affect human health, resulting in memory loss, fatigue, lack of sleep, headaches, etc. [6]. This concern further extends the need for research into microwave and millimeter wave absorbing materials, particularly in the X-band (~8–12 GHz) and Ku-band (~12–18 GHz).

Hexaferrites are iron oxide-based magnetic compounds with a hexagonal crystal structure, divided into six types according to their crystal structure and chemical compositions: M, W, X, Y, Z, and U-type. Magnetically soft hexaferrites (those with a narrow hysteresis loop and low coercivity) and with high permeability, such as Z-type, are considered to be the best hexaferrites suitable for microwave devices functioning in the GHz region. The best known Z-type hexaferrite is $Ba_3Co_2Fe_{24}O_{41}$ (Co_2Z), although the Ba can be substituted by Sr, and Co can be substituted by a range of suitably sized ions. The cobalt-containing Z-type hexaferrites are members of the planar hexaferrite family known asferroxplana, in which the easy magnetisation direction lies in the basal plane of the hexagonal structure perpendicular to the c-axis, or in a cone at an angle to the c-axis, at room temperature [7], and are very soft ferrites as the magnetisation can rotate in this plane/cone. The Z-type crystal structure consists of repeating units of two other hexagonal ferrites, M ferrite ($BaFe_{12}O_{19}$, BaM) and Y ferrite ($Ba_2Co_2Fe_{12}O_{22}$, Co_2Y). Thus, two molecular units M + Y are required to form a single unit of Z-type hexaferrite, which is the member ofthe space group $P6_3/mmc$ [8–10]. Z-type hexaferrites are promising materials for commercial use in high-frequency applications such as telecommunications, radar systems and other microwave devices due to their high ferromagnetic resonance, high thermal stability and relatively high permeability [7,11].

Barium Z-type hexaferrites have been known to have useful microwave properties since their discovery in the early 1960's when they were reported to have a ferromagnetic resonance (FMR) between 1.3 and 3.4 GHz and permeability of up to 9 [7]. It is now established the FMR of Co_2Z is normally around 1.3–1.4 GHz [9,12], although this can be increased slightly with processing optimisation. Recently, Cr substituted Co_2Z was studied by Magham et al. [13] for EMI shielding applications, in which $Ba_3Co_2Cr_xFe_{24-x}O_{41}$ ($x = 0.0, 0.3, 0.6, 0.9$) hexaferrites were prepared using a standard ceramic technique and sintered at 1300 °C for 10 h. These had lowered magnetisation, but FMR increased to around 3 GHz, and absorbed more strongly in the microwave region at ~5 GHz. Shen et al. Fabricated Co_2Z composites coated with silica, and these Co_2Z/SiO_2 composites exhibited good absorption properties between 4 and 14 GHz depending on the number of silica layers, although again at the expense of reduced magnetisation [14].

Strontium Z-type $Sr_3Co_2Fe_{24}O_{41}$ (SrZ) hexaferrite was reported for the first time in 2001 by Pullar and Bhattacharya [15], they found a saturation magnetisation (M_S) of 48.5 A m^2 kg^{-1}, and that it was a very soft ferrite with coercivity (H_C) = 5.6 kA m^{-1}.In oriented polycrystalline SrZ-hexaferrite, the easy axis of magnetisation was found to be in a cone at an angle of 52.3° to the c-axis at RT [16], so it is also a ferox planar type structure. SrZ-hexaferrite has since gained much attention, as not only could it be used as a significant material in microwave frequency devices, but it also has the important magnetoelectric/multiferroic properties [17]. Reported studies show a magnetoelectric/multiferroic-like effect in strontium Z-type hexaferrites even at room temperature and under low magnetic field [18–20]. SrZ-hexaferrite was also reported in 2012 to have an increased FMR compared to Co_2Z,with a broad, poorly defined FMR peak between 2.5 and 3.5 GHz [21]. SrZ-hexaferrite has avery narrow range of formation between a temperature range of 1180–1220 °C, and it decomposesto $SrCo_2Fe_{16}O_{27}$ W-type hexaferrite (SrW) with further heating [22]. As a result, single-phase Z-type hexaferrites are very difficult to prepare [23,24], and the high synthesis temperatures required can lead to an uncontrolled grain growth resulting in discontinuities of the grain size, shape and homogeneity. Thus, it is essential to find a suitable technique and temperature for the synthesis of single-domain SrZ-hexaferrites with a high degree of homogeneity [25]. There are various techniques used for the synthesis of hexaferrites such as ball milling [26], standard ceramic [27,28], microwave hydrothermal [29], co-precipitation [30], micro-emulsion [31] and sol-gel [32,33].

Among all these different synthesis techniques, the sol-gel auto-combustion technique is a low cost and an appropriate technique to prepare a homogeneous product with fine particle size [34].

Strontium hexagallate ($SrGa_{12}O_{19}$) exists as an analogue of $SrFe_{12}O_{19}$ (SrM) ferrite [35], and has been used as a substrate for epitaxial crystal growth of M-type hexaferrites. Single crystals of gallium substituted BaM [36,37], PbM [38] and SrM [39] were studied at GHz frequencies in the 1980's and 1990's, and polycrystalline $PbFe_{12-x}Ga_xO_{19}$ was reported in 2002 [40]. Since then there have been many studies on polycrystalline gallium substituted M-type hexaferrites, such as the work by Trukhanov et al. On Ga substituted BaM [41–48], as well as work by others on gallium mono- and co-substituted M-type hexaferrite [49–54]. In general, increasing Ga substitution in M-type hexaferrite was found to increase H_C and reduce M_S, but the effects on microwave properties were less simple. As the Ga^{3+} concentration in $BaFe_{12-x}Ga_xO_{19}$ increased from $x = 0.1$ to 0.6, the FMR frequency decreased slightly, but as the concentration then increased further to $x = 1.2$, the FMR frequency increased again [41–44,48], with a total variation from 49.1 to 50.4 GHz. The FMR linewidth also increased with x from 3.5 to 5 GHz, indicating a widening of the frequency range where electromagnetic radiation is intensely absorbed, and the shift of the FMR frequency in an applied magnetic field was linear for $x = 1.2$, increasing from 50.5 to 55.5 GHz with an applied field of 0.4 T. Ga substituted BaM was also shown to possess a small ferroics which makes able electrical polarisation, even for values of x as low as 0.1 [47], and giving a spontaneous polarisation of 1-1-5 mC m^{-2} for $x = 0.1$.

There exist a few reported studies of Ga substitution in other

types of hexaferrite, such as W-type [55,56] and Y-type [57]. In 75–140 nm diameter nanopowders of $SrZn_2Ga_xFe_{16-x}O_{27}$ ($x = 0–0.4$) W ferrite made by sol-gel, as expected M_S was found to decrease from 51.0 to 35.8 A m^{-2} kg^{-1} as x increased from 0 to 0.4, but coercivity (H_C) increased significantly with x from 14.6 kA m^{-1} to 76.9 kA m^{-1}, and the loop also became square as the remnant magnetisation (M_r) also increased with the increase of Ga contents (x) [55]. For $x = 0.2$, an FMR frequency of ~2.8 GHz was observed, and a peak absorption of −32dB was seen centered around 8.2 GHz for a 3.4 mm thick sample. For $BaCo_2Ga_xFe_{16-x}O_{27}$ ($x = 0.0–0.8$) W-type hexaferrite made by high energy ball milling, large platy exaggerated grain growth was seen when sintered at 1300 °C, and only a small and irregular variation in Ms with x was observed, with values between 72.5 and 67.7 A m^2 kg^{-1} for $x = 0$ and 0.6, respectively. H_C also exhibited small but irregular variations with x, between 5.6 kA m^{-1} for $x = 0.8–10.3$ kA m^{-1} for $x = 0.2$ [56]. $BaSrCo_2Fe_{11.5}Ga_{0.5}O_{22}$ Y-ferrite was shown to be magnetoelectric at low temperatures, and at room temperature M_S was ~35 A m^2 $kg^{-1}$with a field of 4 T, while the ferrite was very soft with M_r and H_c closed to zero (no precise values given) [57].

There have been several studies reported on $(Ba,Sr)_3Co_2Fe_{24}O_{41}$ [15–20]. However, no study has been reported for Ga substitution of any Z-type hexaferrites. In the present study, we report the effect of Ga substitution on structural, magnetic, dielectric and microwave absorption properties of Z-type $Sr_3Co_{2-x}Ga_xFe_{24}O_{41}$ ($x = 0.0$, 0.4, 0.8, 1.2, 1.6, and 2.0) hexaferrites prepared using a sol-gel auto-combustion technique.

2. Experimental details

2.1. Sample preparation

High purity analytical grade strontium nitrate ($Sr(NO_3)_2$, 99.0% pure, Loba Chemie), cobalt nitrate ($Co(NO_3)_2 \cdot 6H_2O$, 99.99% pure, Merck), gallium nitrate ($Ga(NO_3)_3 \cdot H_2O$, 99.9% pure, Sigma Aldrich), ferric nitrate ($Fe(NO_3)_3 \cdot 9H_2O$, 99% pure, HPLC) and citric acid ($C_6H_8O_7 \cdot H_2O$, 99% pure, HPLC) were used as starting materials. The nitrates and citric acid were used at a 1:1 M ratio.

The stoichiometric amount of metal nitrates were first dissolved in de-ionised water to prepare the nitrate solution. Citric acid was then added to the nitrate solution dropwise. Thereafter, the solution was neutralised by adding ammonia solution (25% w/v, Merck specialities Pvt. Ltd.) slowly to the mixed solution until pH = 7. The prepared solution was continuously stirred while heating to 80 °C, and then maintained at that temperature until the solution transformed to a viscous brown gel. On further heating, the gel started to combust in a self-propagating combustion process to form a loose, fluffy dark brown/blackpowder. Finally, the as-synthesised powder was preheated in a muffle furnace to550 °C to remove any remaining organics impurities, followed by 1200 °C for 5 h in order to obtain the Z-type hexaferrite powder. Fig. 1 represents a flowchart to prepare Z-type $Sr_3Co_{2-x}Ga_xFe_{24}O_{41}$ hexaferrite powder samples.

2.2. Characterisation

The Fourier-Transform infra-red (FTIR) spectra of all heated samples were recorded at room temperature by placing a small quantity of finely ground powder on a sample holder on a FTIR Spectrometer (PerkinElmer LS 55) over the wave number range of 4000–400 cm^{-1}.

The phase purity and crystal structure of all samples were examined at room temperature by X-ray diffraction (XRD) technique (Rigaku Geiger flex system) using Cu-K_α radiation, λ = 1.5406 Å with 2θ *varying from* 20-80° instep-scan 0.02°. The

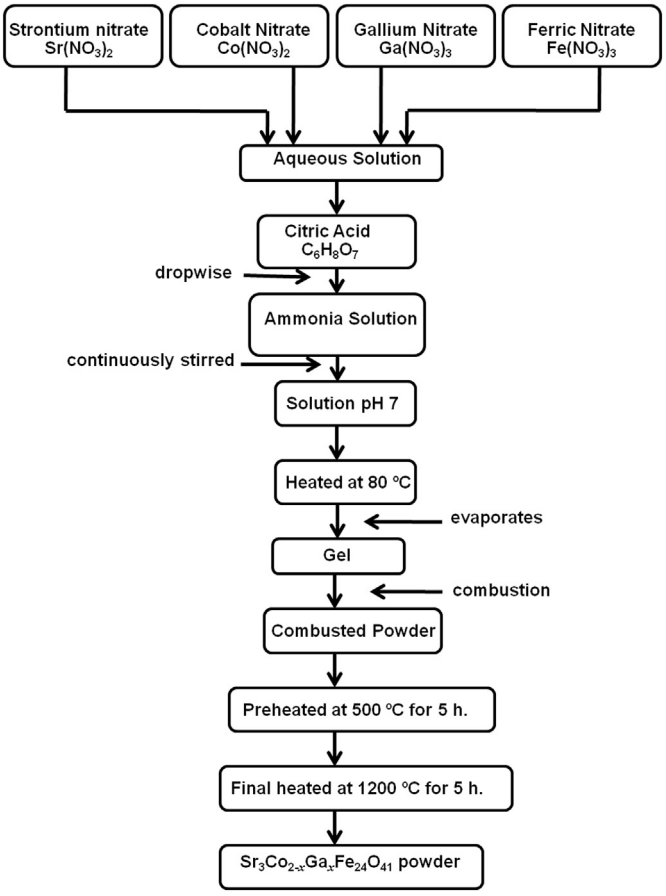

Fig. 1. Flowchart shows the sample preparation of $Sr_3Co_{2-x}Ga_xFe_{24}O_{41}$ hexaferrite powder.

unit cell volume (V_{cell}) value of heated samples was calculated using an equation (1) [58].

$$\boldsymbol{V_{cell} = (0.866)\, a^2 c} \tag{1}$$

An average crystallite size (D_{xrd}) for all samples was calculated from the high intensity peak of XRD pattern using Scherrer's equation [59]:

$$D_{xrd} = \frac{0.9\lambda}{\beta_{1/2}\cos\theta} \tag{2}$$

where, λ is the X-ray wavelength (1.5406 Å), $\beta_{1/2}$ is FWHM of the diffraction peak in degree, andθ is the Bragg angle in degrees.

Bulk density (d_B) was calculated by the following relation [60].

$$dB = \frac{\boldsymbol{m}}{\boldsymbol{\pi r^2 h}} \tag{3}$$

where, m is mass of a pellet, r is the radius of a pellet and h is the thickness of a pellet.

The X-ray density (d_x) was calculated using the following equation [58]:

$$d_x = \frac{\boldsymbol{ZM}}{\boldsymbol{N_A V_{cell}}} \tag{4}$$

where, Z is the number of molecules per unit cell = 2 for Z-type

hexaferrites, M = molecular weight and N_A = Avogadro's number = 6.023×10^{23}.

The porosity (P) of the material was calculated using equation (5) [58].

$$P(\%) = \left(1 - \frac{d_B}{d_x}\right) \times 100\% \quad (5)$$

The surface morphology of heated samples was examined by two different instruments - a Phenom ProX scanning electron microscope (SEM) and TECSCAN field emission scanning electron microscope (FE-SEM).

Magnetic hysteresis loops (M – H curves) of $Sr_3Co_{2-x}Ga_xFe_{24}O_{41}$ hexaferrites were recorded at 5 K and 300 K using a SQUID magnetometer (Quantum Design, MPMS5). To observe the samples' ***low temperature*** magnetic properties, measurements were carried out at 5 K and 300 K under an applied field of 100 Oe and 1000 Oe, respectively. In zero-field cooled (ZFC) measurements, samples were cooled to 5 K in the absence of magnetic field, and the magnetic field of 100 Oe or 1000 Oe (0.01T or 0.1T) was applied and magnetisation was recorded as the sample was heated up to 300 K. For field cooled (FC) measurements, the samples were cooled down from 300 K to 5 K under magnetic field of 100 Oe or 1000 Oe (0.01 T or 0.1 T), and magnetisation was recorded.

A conventional spectrometer operating in constant acceleration mode in transmission geometry with Co^{57} source in Rh matrix of 50 mCi was used to record the Mössbauer spectra. These spectra were fitted using the Win-Normos site fit program. An enriched α-^{57} Fe metal foil was used to calibrate the velocity scale. The isomer shift values are relative to Fe metal foil ($\delta = 0.0$ mm/s).

The quadrupole splitting (Δ) of a sextet is calculated using the following equation [61,62]:

$$(\Delta) = \tfrac{1}{4}\, eqQ(3\cos^2\theta - 1) \quad (6)$$

where θ = angle between the direction of the hyperfine magnetic fields and the principal axis of the electric field gradient (EFG), Q = nuclear quadrupole moment, and q = z-component of the EFG along the principal axis.

The number of Bohr magnetons (n_B) of the compositions was calculated using Eq. (7) [63]:

$$n_B = \frac{Molecular Weight \times M_s}{NB} \quad (7)$$

where, N = Avogadro's number = 6.023 $mol^{-1} \times 10^{23}$ and B = 9.2740 $\times 10^{-21}$ erg T^{-1}

The low-frequency dielectric measurements were performed at room temperature within a 100 Hz to 2 MHz frequency region, using a Precision LCR meter (Agilent E4980A).

The real dielectric constant (ε')is measured by using equation (8):

$$\varepsilon' = \frac{C_p t}{\varepsilon_0 A} \quad (8)$$

where, C_p = capacitance (farad), t = thickness of the pellet (m), A = cross-sectional area of the electrode (m^2), and ε_0 = the permittivity of free space.

The AC conductivityσ_{ac})is calculated using equation (9):

$$\sigma_{ac} = \frac{2\pi f t C_p \tan\delta}{A} \quad (9)$$

where, A = area of the electrode, t = thickness of the sample, C_p = capacitance.

The electrical modulus (M) with respect to real (M') and imaginary (M'') components were calculated using equation (10):

$$(M) = (M' + M'') \quad (10)$$

where, $(M') = \frac{\varepsilon'(\omega)}{[\varepsilon'(\omega)]^2 + [\varepsilon''(\omega)]^2}$ *and* $(M'') = \frac{\varepsilon''(\omega)}{[\varepsilon'(\omega)]^2 + [\varepsilon''(\omega)]^2}$

High-frequency complex permittivity and permeability measurements of all samples were carried out at room temperature for electromagnetic evaluation at microwave frequencies in the range of 8–12.50 GHz, with a Microwave Network Analyzer (Agilent N5231 PNA-L) using a coaxial termination with an APC-7 connector as a sample holder.

3. Results and discussion

3.1. Fourier-transform infrared spectroscopy (FTIR) analysis

Fig. 2 (a) represents the FTIR spectra of $Sr_3Co_{2-x}Ga_xFe_{24}O_{41}$ (x = 0.0, 0.4, 0.8, 1.2, 1.6 and 2.0). The FTIR spectra of all samples show two strong characteristic absorption bands (ν_1) and (ν_2) between the range of 400–600 cm^{-1} confirming the formation of ferrites. The absorption band between 415 and 480 cm^{-1} corresponds to the metal-oxygen vibrations in octahedral B-sites (ν_2);

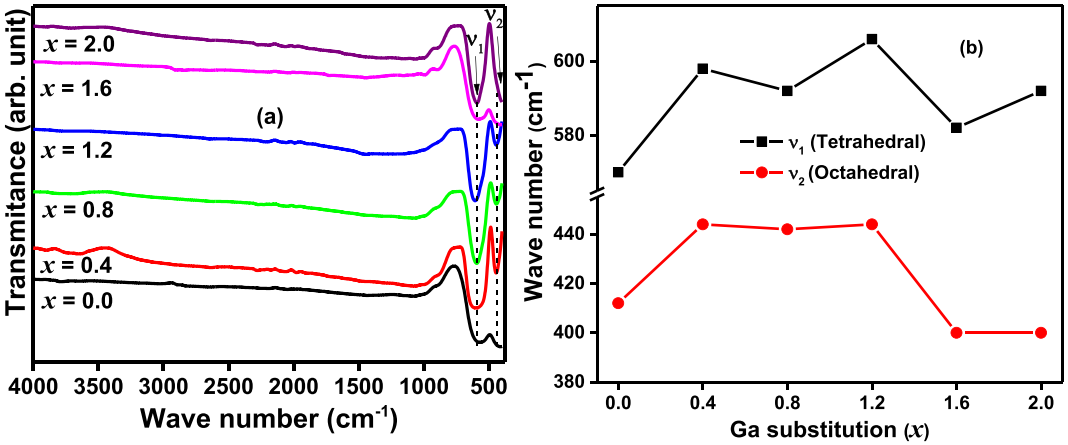

Fig. 2. (a) FTIR spectra of $Sr_3Co_{2-x}Ga_xFe_{24}O_{41}$ (x = 0.0, 0.4, 0.8, 1.2, 1.6 and 2.0) hexaferrite powder samples heated at 1200 °C for 5 h.(b) Variation in vibrations with Ga substitution (x) of tetrahedral (ν_1) and octahedral (ν_2) metal-oxygen bonds.

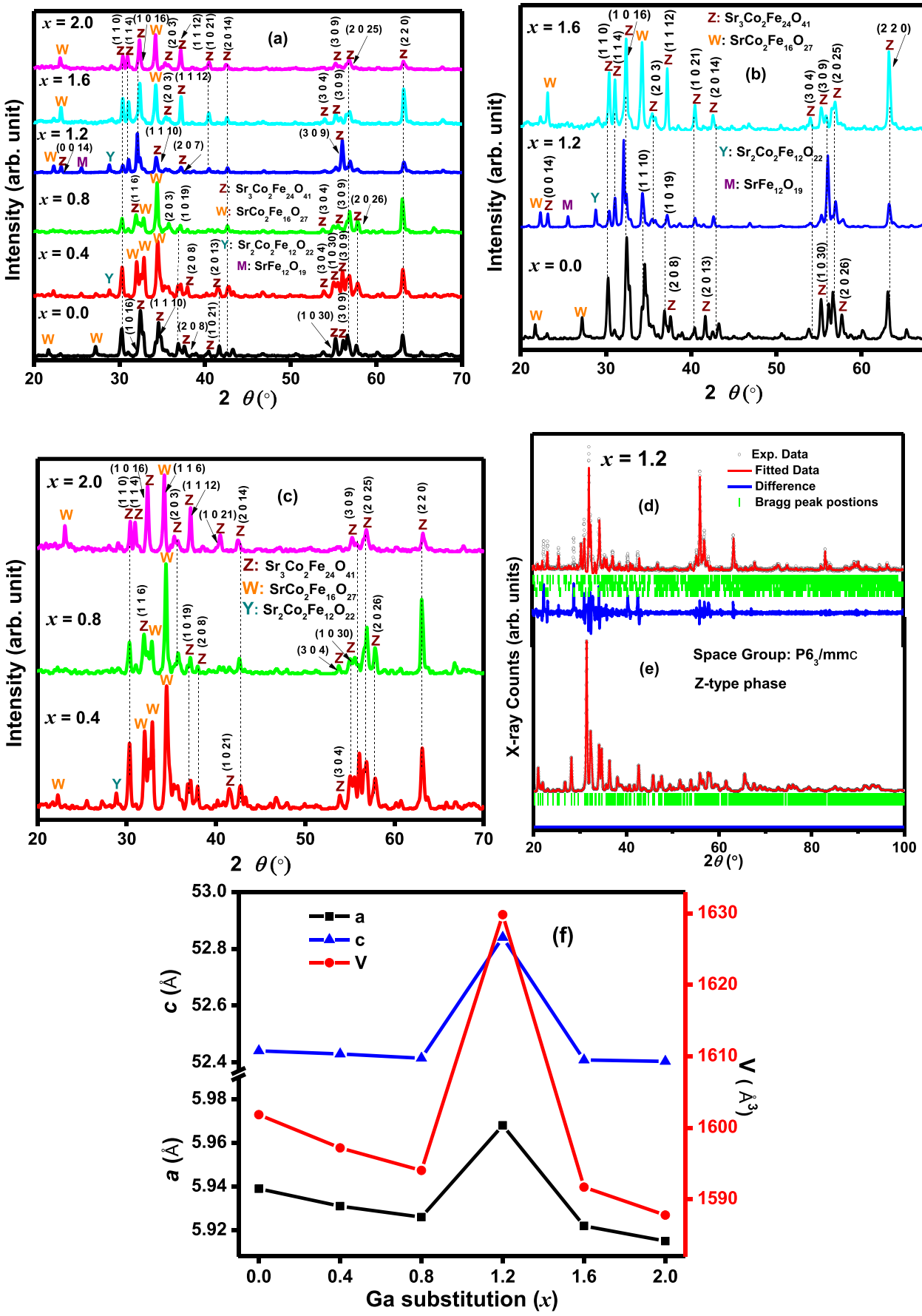

Fig. 3. (a). XRD patterns of $Sr_3Co_{2-x}Ga_xFe_{24}O_{41}$ (x = 0.0, 0.4, 0.8, 1.2, 1.6, and 2.0) samples heated at 1200 °C for 5 h. For easier comparison, selected patterns are compared for (b) x = 0.0, 1.2 and 1.6, (c) x = 0.4, 0.8 and 2.0 hexaferrite powder samples. (d) The Rietveld refined profile fit XRD pattern (2θ = 20–100°) of x = 1.2. (e) The Rietveld refined XRD pattern generated (calculated) of pure Z-type phase.(f) The variation of lattice constants (a, c) and unit cell volume (V) with Ga substitution (x).

Table 1
Percentage of various phases present in $Sr_3Co_{2-x}Ga_xFe_{24}O_{41}$ (x = 0.0, 0.4, 0.8, 1.2, 1.6, and 2.0) hexaferrite powder samples heated at 1200 °C for 5 h.

Ga content (x)	Percentage of Phases			
	Z-Phase (% ± 2)	W-Phase (% ± 2)	Y-phase (% ± 2)	M-Phase (% ± 2)
0.0	94	6	0	0
0.4	72	26	2	0
0.8	76	24	0	0
1.2	89.5	3.4	2.6	4.5
1.6	84	16	0	0
2.0	78	22	0	0

Table 2
Lattice constants, c/a ratio, FWHM, unit cell volume and average crystallite size of $Sr_3Co_{2-x}Ga_xFe_{24}O_{41}$ (x = 0.0, 0.4, 0.8, 1.2, 1.6, and 2.0) hexaferrite powder samples, heated at 1200 °C for 5 h.

Ga content	2θ	Lattice constants		(c/a) ratio	FWHM	Unit cell volume	Average crystallite size
(x)	(°)	a (Å)	c (Å)		(°)	V (Å^3)	D_{xrd} (nm)
0.0	32.438	5.939	52.441	8.8299	0.4005	1601.826	21.59
0.4	34.459	5.931	52.43	8.8399	0.362	1597.179	24.00
0.8	34.39	5.926	52.415	8.8449	0.2705	1594.031	32.12
1.2	32.081	5.968	52.84	8.8538	0.2149	1629.815	40.19
1.6	32.362	5.922	52.409	8.8498	0.29	1591.697	29.80
2.0	34.2	5.915	52.404	8.8595	0.2611	1587.785	33.26

while, the band around 550-600 cm^{-1} corresponds to the metal-oxygen vibrations in tetrahedral A-sites (ν_1) in the hexagonal lattice, which attributes to the Fe^{3+}-O^{2-} vibrations in tetrahedral and octahedral sites [64].

No other characteristic bands were observed, which confirms that prepared samples are free from organic residue and anionic impurities. The values of (ν_1)are greater than (ν_2) as the vibration of the tetrahedral group is higher than that of the octahedral group, which ascribes the smaller bond length to the A-site groups than to the B-site groups [65,66].The position and intensities of (ν_1) and (ν_2) are found to vary slightly with Ga substitution, which is due to the difference in the distances for the tetrahedral and octahedral ions [67]. Fig. 2(b) represents the variation in (ν_1)and (ν_2) with Ga substitution of tetrahedral (ν_1) and octahedral (ν_2) metal-oxygen bonds. The values of (ν_1) and (ν_2) were found to vary with Ga substitution, which may be due to change in Fe—O stretching at both sites due to the larger atomic mass of Ga (~69.72 amu) compared with that of Co^{2+}(~58.93 amu).

The inconsistency in the variation trend of ν_1 and $\nu_2$with Ga substitution can be attributed to the method of preparation, the grain size and sintering temperature [68]. The slight variation in the band position for the different compositions of $Sr_3Co_{2-x}Ga_xFe_{24}O_{41}$ is due to the difference in distances between tetrahedral (ν_1) and octahedral (ν_2) ions. These bands can be interpreted on the basis of tetrahedral and octahedral position. This is due to the Fe—O stretching vibration band [69,70].

3.2. X-ray diffraction analysis

Fig. 3(a) depicts the XRD patterns of $Sr_3Co_{2-x}Ga_xFe_{24}O_{41}$ (x = 0.0, 0.4, 0.8, 1.2, 1.6, and 2.0) hexaferrite samples prepared using the sol-gel auto-combustion method and heated at 1200 °C for 5 h. XRD patterns were indexed using winPLOTR software. All observed peaks were compared with standard JCPDS file no. 19-0097of Z-type hexaferrite crystal structure with space group $P6_3/mmc$ ($a = b$ = 5.88 Å, c = 52.31 Å and V = 1566.28 Å^3). Percentage of various phases and structural parameters of heated samples are listed in Table 1 and Table 2 respectively. It is known that Z-type hexaferrite is composed of alternate stacks of Y and M-type hexaferrites [71]. Fig. 3 (b) shows the XRD patterns of x = 0.0, 1.2 and 1.6 samples, which revealed the formation of Z-phase along with minor peaks of W-phase (JCPDS file no. 78—0135, $a = b$ = 5.899 Å and c = 32.846 Å). The XRD patterns of x = 0.4, 0.8 and 2.0 samples (Fig. 3 (c)) show mixed phases of Z and W, where the high-intensity peak is indexed with W-phase. A single peak of

Table 3
The X-ray density, Bulk density, and the Porosity of $Sr_3Co_{2-x}Ga_xFe_{24}O_{41}$ (x = 0.0, 0.4, 0.8, 1.2, 1.6, and 2.0) hexaferrite samples heated at 1200 °C for 5h.

Ga content (x)	X-ray density dx (g/cm3)	Bulk density dB (g/cm3)	Porosity P (%)
0.0	4.927	3.758	23.8
0.4	4.950	3.823	22.7
0.8	4.969	3.741	24.6
1.2	4.869	3.711	23.8
1.6	4.994	3.688	26.2
2.0	5.018	2.667	46.9

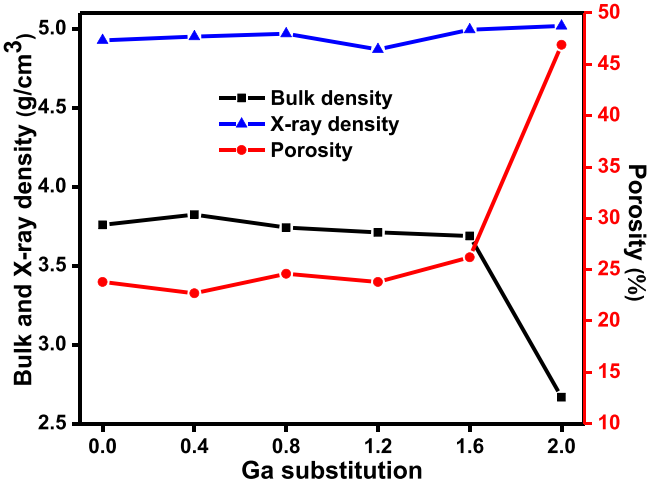

Fig. 4. Variation of the bulk, X-ray density, and porosity with Ga substitution (x).

Y-type hexaferrite (JCPDS file no. 44–0206, $a = b = 5.859$ Å and $c = 43.504$ Å) was observed in $x = 0.4$ and 1.2 samples, and one peak of the M-phase (JCPDS file no. 84–1531, $a = b = 5.884$ Å and $c = 23.049$ Å) was also present in $x = 1.2$ composition.

Interestingly, for compositions $x = 0.0$, 1.2 and 1.6, the highest intensity X-ray diffraction peak is observed at 2θ ~32° and its (h k l) value is indexed to (1 0 16), which is in good agreement with the standard file of Z-type hexaferrites (JCPDS file no. 19–0097). However, for compositions $x = 0.4$, 0.8 and 2.0, the highest intensity peak is observed to be shifted to 2θ~34° with (h k l) value (0 0 20), but the intensity didn't matched with the standard file for unsubstituted Z-type hexaferrites.

The relative intensity of this diffraction peak with (hkl) - (1 0 16) tends to decrease from $x = 0.0$ to 0.8, and then in $x = 1.2$ and 1.6 it again increases to high intensity. All samples showed the Z-phase as the main phase (Table 1).The Rietveld refined profile fit of the XRD pattern ($2\theta = 20$–100 deg.) of $x = 1.2$ is shown in Fig. 3(d), and the generated (calculated) pattern of pure Z-type phase is also

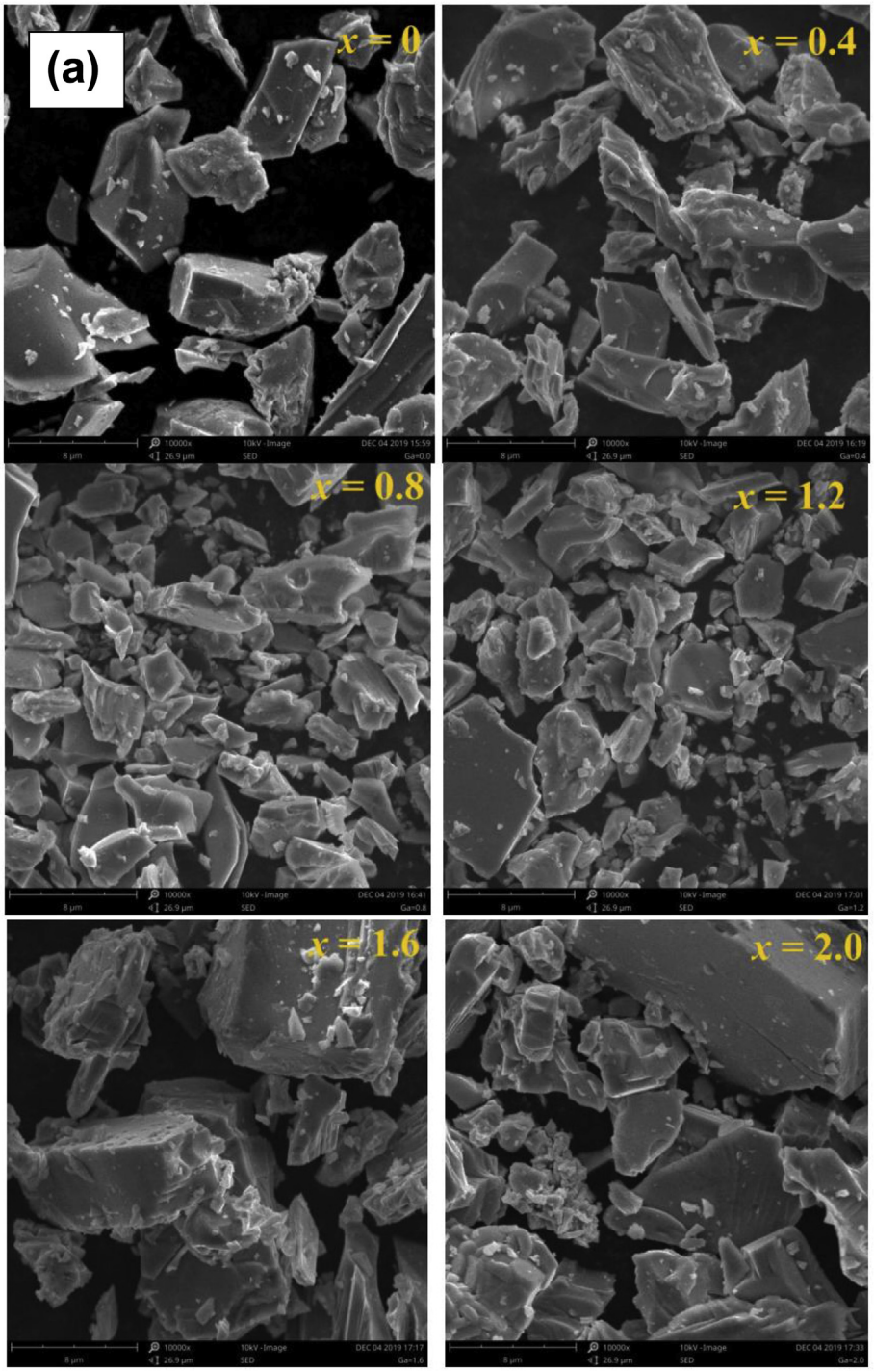

Fig. 5(a). SEM images of $Sr_3Co_{2-x}Ga_xFe_{24}O_{41}$ ($x = 0.0$, 0.4, 0.8, 1.2, 1.6, and 2.0) hexaferrite samples heated at 1200 °C for 5 h. The images were recorded on a Phenom ProX Desktop SEM with 8 μm scale bar.

shown in Fig. 3(e). The Rietveld refined profile of $x = 1.2$ is fitted with three phases (Z-type, W-type and M-type). 89.5% is Z-type phase, and the remaining 10.5% is made up of W-type, M-type and Y-type phases as listed in Table 1.

Further, there is a slight decrease in intensity in the composition $x = 2.0$. This reveals that the crystal symmetry of compositions $x = 0.4$, 0.8 and 2.0 is affected due to the presence of the secondary phase (W-type). Thus, the highest intensity peak of samples $x = 0.4$, 0.8 and 1.2 which is shifted to 34° is indexed with (hkl) value (1 1 6), which is in good agreement with the standard file of W-type hexaferrites (JCPDS file no. 78−0135).

It is known that single phase strontium Z-type hexaferrites have

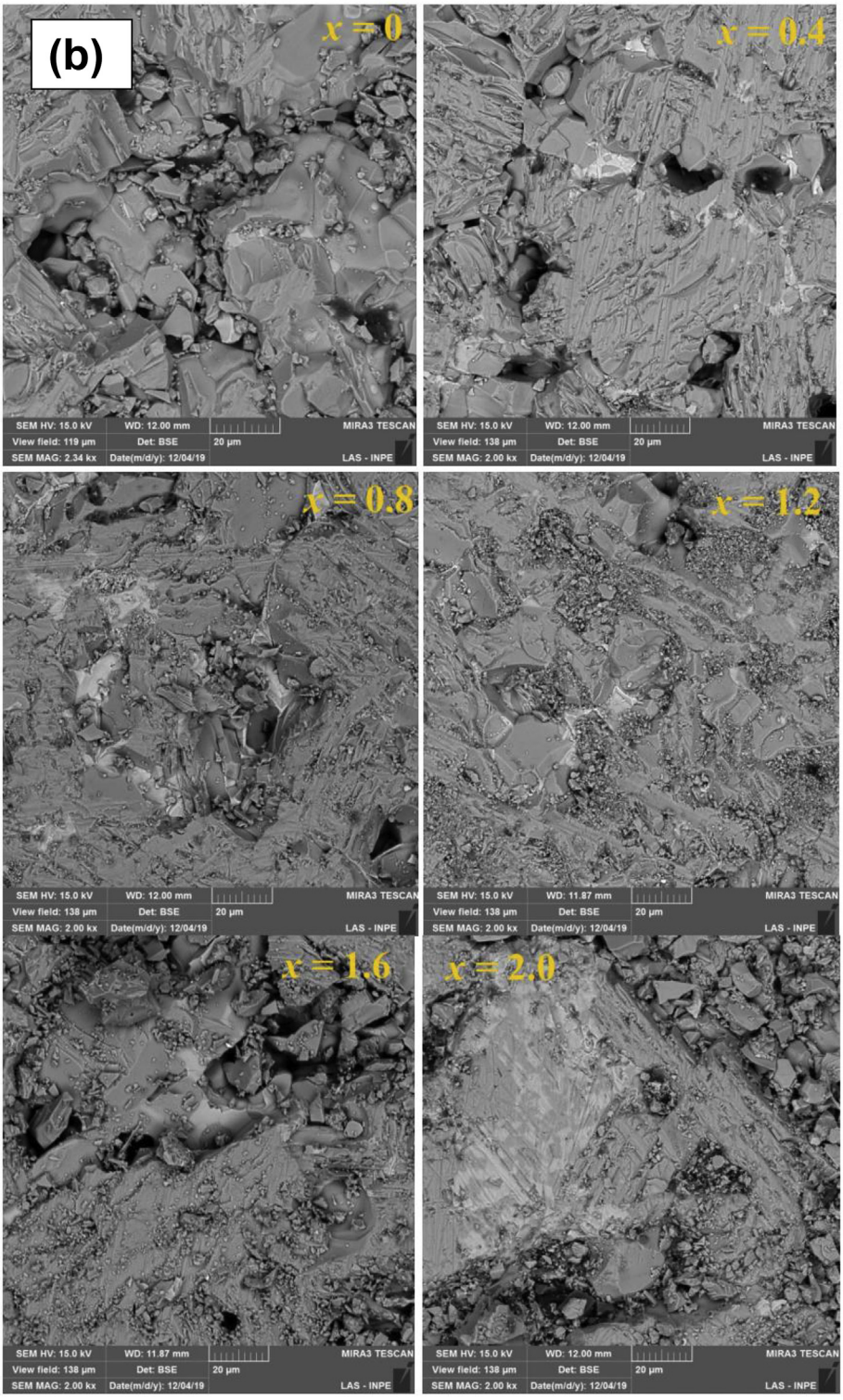

Fig. 5(b). FE-SEM images of $Sr_3Co_{2-x}Ga_xFe_{24}O_{41}$ ($x = 0.0$, 0.4, 0.8, 1.2, 1.6, and 2.0) hexaferrite samples heated at 1200 °C for 5 h. The images were recorded on a TESCAN SEM with 20 μm scale bar.

a very narrow formation range of about 1180–1200 °C [20], and in the present study, the samples were heated at 1200 °C for 5 h, which is on the border of this, so it could be expected to contain some amount of W-phase. Generally, Z-type hexaferrite decomposes to W-type ferrite at higher temperatures [9]. It is clear from Table 1 that the percentage of W- phase is found to be minimum (3.4%) in $x = 1.2$, although this secondary phase is accompanied by an amount of Y (2.6%) and M-phases (4.5%), while the maximum percentage of W-phase (26%) is found in the $x = 0.4$ composition.

The values of lattice constants, unit cell volume, full width at half maximum (FWHM) and crystallite size with Ga substitution (x) are listed in Table 2.

The variation of lattice constants and unit cell volume with Ga substitution is presented in Fig. 3(f). It is clear from Table 2 and Fig. 3(f) that lattice parameters ('a', 'c') and cell volume 'V' decrease with Ga content, except in $x = 1.2$.These variations observed in the lattice parameters 'a', 'c' and unit cell volume 'V' with the substitution of Ga ions are due to the different ionic radii of substituted Ga^{+3} (0.62 Å) and host ions Co^{2+} (0.72 Å) [72]. The c/a ratio for all Z-type hexaferrite samples was found to be in the expected range of 8.82–8.86 [73]. As Ga content (x) increased from 0.0 to 1.2, the crystallite size was found to increase from 22 nm to 40 nm, then it was found to decrease to 30 nm for $x = 1.6$, and 33 nm for $x = 2.0$. The values of lattice parameters, unit cell volume and crystallite size of sample $x = 1.2$ are found to be quite high compared to other samples, which may be due to the presence of three secondary phases of M, Y and W, along with the Z-phase.

It is very difficult to get the pure Z-type phase. Here, the impurities mean the secondary phases of hexaferrites only. There is no

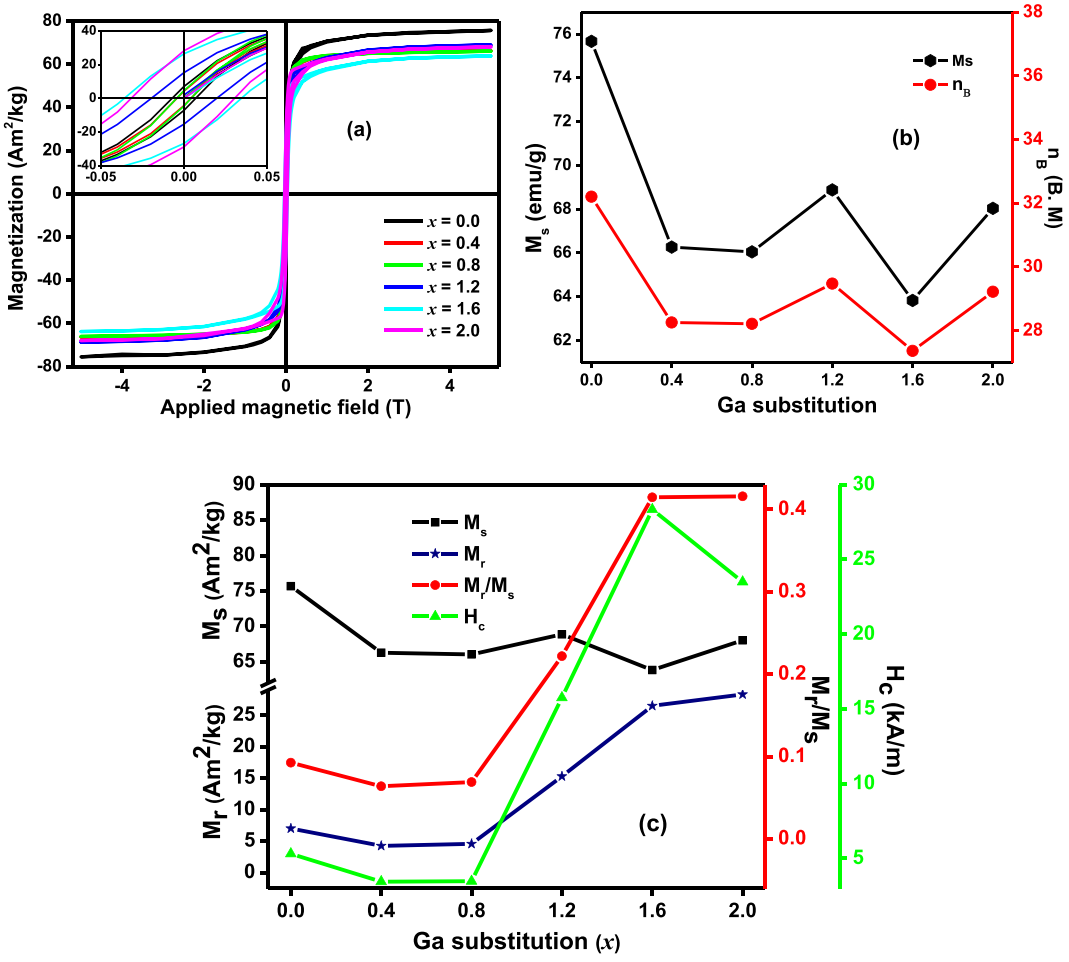

Fig. 6. (a). Magnetic hysteresis loops of $Sr_3Co_{2-x}Ga_xFe_{24}O_{41}$ ($x = 0.0, 0.4, 0.8, 1.2, 1.6$, and 2.0) hexaferrite powder samples heated at 1200 °C for 5 h, recorded at 300 K, (b) Variation of n_B and M_S with Ga substitution (x), (c) Variation of saturation magnetisation (M_S), remanent magnetisation (M_r), coercive field (H_C) and squareness ratio (M_r/M_S) with Ga substitution (x).

Table 4
Magnetic parameters at 300 K of $Sr_3Co_{2-x}Ga_xFe_{24}O_{41}$ ($x = 0.0, 0.4, 0.8, 1.2, 1.6$ and 2.0) hexaferrite powder samples heated at 1200 °C for 5 h.

Ga content (x)	Saturation magnetisation M_S (A m^2kg^{-1})	Remanent magnetisation M_r (A m^2 kg^{-1})	M_r/M_S	Coercivity H_C (kA m^{-1})	Coercivity H_C (Oe)
0.0	75.67	7.00	0.09	5.3	66
0.4	66.27	4.24	0.06	3.4	43
0.8	66.05	4.56	0.07	3.5	44
1.2	68.88	15.28	0.22	15.8	198
1.6	63.83	26.48	0.41	28.3	355
2.0	68.04	28.30	0.42	23.5	295

unknown peak, organic residue or any kind of impurities due to incomplete reaction present. The M-phase is a necessary precursor to the Z phase, and the W-phase is a common decomposition product of the Z-phase. With the very narrow synthesis window for SrZ ferrites, it is difficult to obtain pure phase SrZ ferrites. Also, although the mixed hexaferrite phases are present, the high Ms and low Hc characteristics in the present study are suitable for various applications such as data recording [33], stealth technology [74] and absorption of the energy of electromagnetic waves [75]. Yutaro Kitagawa et al. [76] reported the Low-field magnetoelectric effect at room temperature in $Sr_3Co_2Fe_{24}O_{41}$ polycrystalline ceramics in *Nature Materials*. This sample was not pure phase, it consisted of W and U-type phases along with Z-type phase.

3.3. Physical properties

Density plays a key role in investigating the physical properties of magnetic ceramics. The calculated values of X-ray density, bulk density and porosity are listed in Table 3, and Fig. 4 represents the variation in X-ray density, bulk density and porosity as a function of Ga content (x).

It is clear from Table 3 that X-ray density increases from 4.927 g/cm^3 to 5.018 g/cm^{3}as Ga content (x) increases, except in the sample $x = 1.2$. This increasing trend of X-ray density is attributed to the greater atomic mass of substituted Gallium ions (69.723 amu) compared to the host cobalt ions (58.933 amu) [77]. The values of bulk density decrease as Ga content increases except sample $x = 0.4$. This decreasing behaviour of bulk density is depicted to the smaller density of Ga^{3+} (5.91 g/cm^3) as compared to that of Co^{2+} (8.86 g/cm^3) cations [77]. Porosity increases as Ga content ($x > 0.0$) increases due to the decrease in bulk density. The values of bulk density were found to be less than the X-ray density, which is due to the presence of pores produced during heat treatment [77].

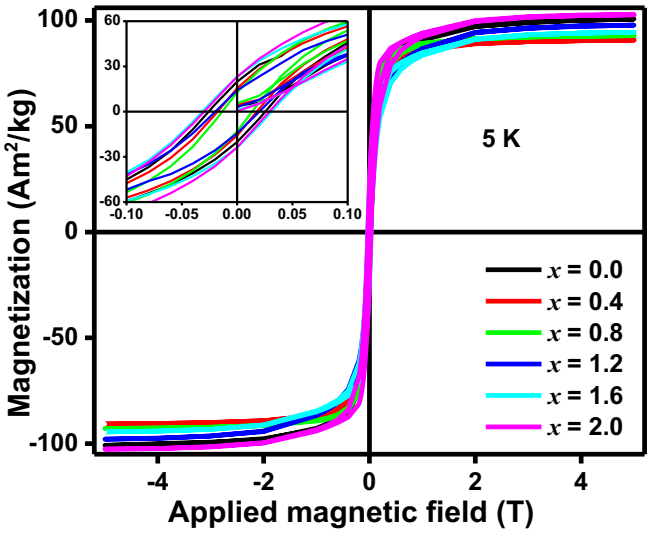

Fig. 7. Magnetic hysteresis loops recorded at 5K of $Sr_3Co_{2-x}Ga_xFe_{24}O_{41}$ ($x = 0.0, 0.4, 0.8, 1.2, 1.6$, and 2.0) hexaferrite powder samples heated at1200 °C for 5h.

3.4. Surface morphology

Fig. 5(a and b) represents the SEM micrographs of $Sr_3Co_{2-x}Ga_xFe_{24}O_{41}$ ($x = 0.0, 0.4, 0.8, 1.2, 1.6$, and 2.0) hexaferrite samples heated at 1200 °C for 5 h, recorded on two different instruments. It is clear from Fig. 5(a and b) that each sample possesses different surface morphology. The observed grain clusters are non-uniform, inhomogeneous and agglomerated.

3.5. Magnetic properties

3.5.1. Hysteresis loops

Hysteresis loops (M − H curves) of $Sr_3Co_{2-x}Ga_xFe_{24}O_{41}$ ($x = 0.0$, 0.4, 0.8, 1.2, 1.6 and 2.0) hexaferrite samples were recorded at room temperature (300 K) under an applied field of ± 5T and are shown in Fig. 6 (a). The values of saturation magnetisation (M_S), remanent magnetisation (M_r), coercivity (H_C) and squareness ratio (M_r/M_S) are calculated from the hysteresis loops and summarised in Table 4. The inset of Fig. 6 (a) shows the enlarged view of coercivity, from −0.05T to + 0.05T. All samples show the typical soft ferrite characteristics with low coercivity (H_C = 43 Oe to 355 Oe = 3.4–28.3 kA m^{-1}).

The variation of n_B and M_S with Ga content is shown in Fig. 6 (b). Magnetic moment n_B exhibits a similar nature to M_S. Ga substituted samples show a decreasing trend compared to the pure ($x = 0.0$) sample, as magnetic moment is the main mechanism for the variation of M_S. Table 4 and Fig. 6 (c) shows the variation of saturation magnetisation (M_S), remanent magnetisation (M_r), coercive field (H_C) and squareness ratio (M_r/M_S) with Ga substitution (x). M_S occurs when all the magnetic dipoles are aligned.

The saturation magnetisation is found to decrease with x and remains more or less stable at around 66 A m^{2}kg^{-1} for $x = 0.4$–1.2, which further drops to 64 A m^{2}kg^{-1} for $x = 1.6$ sample and again increases slightly for fully Ga substituted $x = 2.0$ (~68 A m^2 kg^{-1}). However, *in all cases* M_S value has decreased after substituting Ga. These larger than expected values of M_S (if only a Z ferrite) suggest the presence of SrW phase [78,79]. XRD analysis supports the formation of SrW phase. This value of M_S closely matches with the reported value by Jijing Xu et al. [80], and high M_S values around 78.8–81.3 emu/g. was also reported for W-type hexaferrites by Jae-Hyoung You et al. [81].

It is clear from Fig. 6 (c) that in general coercivity (H_C) increases with greater Ga substitution, although for the samples with only a little substitution there is in fact an initial small decrease in H_C. With $x > 0.8$ H_C increases, although with the fully Ga substituted sample ($x = 2.0$) as there is a slight decrease in H_C values compared to the $x = 1.6$ sample. Remanent magnetisation (M_r) decreases initially for $x = 0.4$ composition and then it uniformly increases with further Ga substitution. The increase in H_C is directly related to an anisotropy field (H_a) [82], but will also be optimised in samples whose grain size is close to the single magnetic domain size,

Table 5
Magnetic parameters at 5K of $Sr_3Co_{2-x}Ga_xFe_{24}O_{41}$ ($x = 0.0, 0.4, 0.8, 1.2, 1.6$ and 2.0) hexaferrite powder samples heated at 1200 °C for 5h.

Ga content (x)	Saturation magnetisation M_S (A m^{2}kg^{-1})	Remanent magnetisation M_r (A m^2 kg^{-1})	M_r/M_S	Coercivity H_C (kA m^{-1})	Coercivity H_C (Oe)
0.0	100.72	19.87	0.20	20.4	256
0.4	90.71	15.53	0.17	14.0	176
0.8	92.84	12.79	0.14	10.8	135
1.2	97.77	14.16	0.14	15.3	191
1.6	94.45	23.13	0.24	25.1	315
2.0	102.73	23.12	0.23	25.4	318

preventing domain wall movement contributions. This overall increment of coercivity values with Ga substitution suggests that the material's magnetic hardness can be tuned. Faiza Aen et al. also reported the increase in coercivity by Ga substitution in W-type hexaferrite [55]. The values of H_C lie in the range of 3.4–28.3 kA m^{-1} (43-356Oe), which demonstrates that these are all soft ferrites. The squareness ratio (M_r/M_S) lies in the range of 0.06–0.42, which indicates the formation of a multi-domain structure.

Fig. 7 shows the hysteresis loops recorded at 5 K, and the values of magnetic parameters are given in Table 5. At 5 K,the samples show similar trends in H_C, although all have relatively higher coercive field values as compared to room temperature, except for the $x = 1.6$ composition. As expected, M_S values are all greater at 5 K, but all are close to the values for the unsubstituted samples ($x = 0.0$), and in the case of the fully substituted $x = 2.0$, slightly

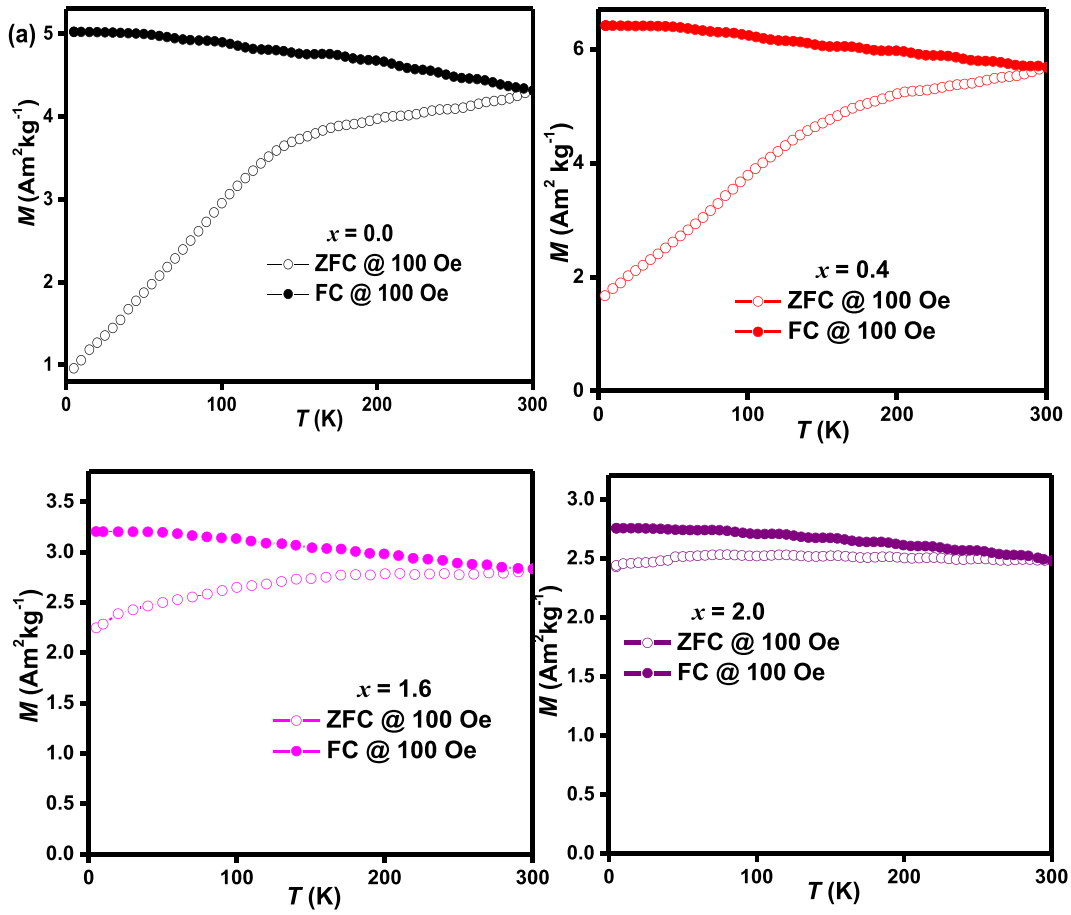

Fig. 8(a). ZFC-FC curves in an applied magnetic field of 100 Oe for typical $Sr_3Co_{2-x}Ga_xFe_{24}O_{41}$ ($x = 0.0$, 0.4, 1.6 and 2.0) hexaferrite powder samples heated at 1200 °C for 5 h.

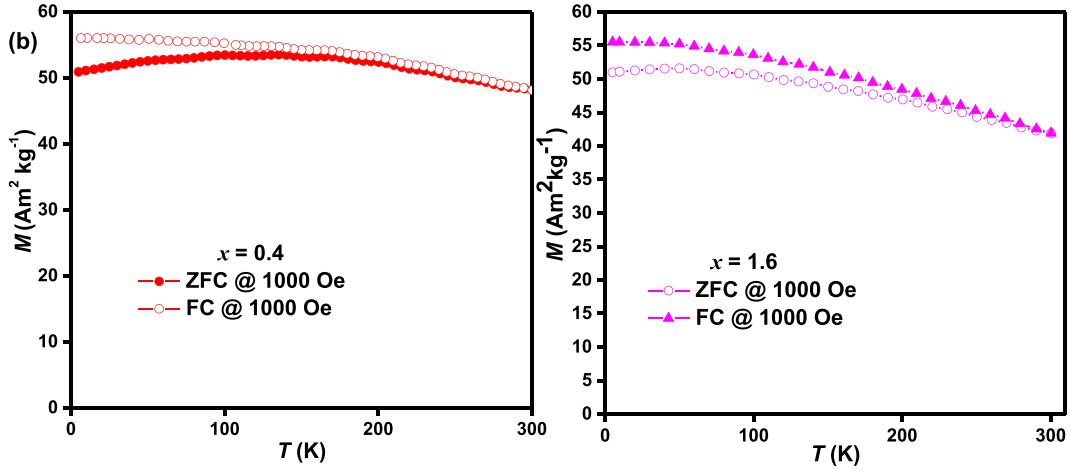

Fig. 8(b). ZFC-FC curves recorded under an applied magnetic field of 1000 Oe for $Sr_3Co_{2-x}Ga_xFe_{24}O_{41}$ ($x = 0.4$ and 1.6) hexaferrite powder samples heated at 1200 °C for 5 h.

Table 6
The values of hyperfine field (H_{hf}), isomer shift (δ), quadrupole splitting (Δ), line width (Γ) and relative area (R_A) of tetrahedral (tetra), octahedral (octa) and trigonal bypiramidal (tbp) sites of Fe^{3+} ions for Ga substituted $Sr_3Co_{2-x}Ga_xFe_{24}O_{41}$ (x = 0.0, 0.4, 0.8, 1.2, 1.6, and 2.0) hexaferrites derived from Mössbauer spectra recorded at room temperature. *Isomer shift values are with respect to α-Fe metal foil.

Ga-content (x)	Iron sites	Ionic state (high spin)	Relative area (R_A) (%)	Isomer shift* (δ) mm/s ±0.01	Quadrupole splitting (Δ) mm/s ±0.02	Hyperfine field (H_{hf}) Tesla ±0.1	Outer line width (Γ) mm/s ±0.05	Fitting quality (χ^2)
0.0	Sextet-A	Fe^{3+}	9.7	0.389	−0.094	52.532	0.291	1.35
	Sextet-B	Fe^{3+}	15.9	0.469	0.052	50.216	0.409	
	Sextet-C	Fe^{3+}	29.1	0.219	−0.042	49.574	0.487	
	Sextet-D	Fe^{3+}	3.8	0.321	0.349	41.638	0.199	
	Sextet-E	Fe^{3+}	17.8	0.364	−0.309	40.672	0.856	
	Sextet-F	Fe^{3+}	22.7	0.366	−0.154	39.450	0.449	
	Doublet	Fe^{3+}	1.0	0.241	0.528	–	0.554	
0.4	Sextet-A	Fe^{3+}	12.1	0.388	−0.090	52.325	0.3441	1.23
	Sextet-B	Fe^{3+}	12.1	0.495	0.053	50.004	0.309	
	Sextet-C	Fe^{3+}	25.3	0.222	−0.082	49.426	0.4505	
	Sextet-D	Fe^{3+}	0.6	0.162	0.030	41.195	0.230	
	Sextet-E	Fe^{3+}	3.0	0.289	−0.876	42.697	0.257	
	Sextet-F	Fe^{3+}	46.0	0.369	−0.202	39.757	0.618	
	Doublet	Fe^{3+}	0.9	0.185	0.539	–	0.613	
0.8	Sextet-A	Fe^{3+}	10.2	0.351	−0.060	52.075	0.302	1.3
	Sextet-B	Fe^{3+}	17.0	0.435	0.075	50.031	0.532	
	Sextet-C	Fe^{3+}	23.0	0.193	−0.016	49.156	0.452	
	Sextet-D	Fe^{3+}	5.6	0.323	0.400	41.156	0.244	
	Sextet-E	Fe^{3+}	3.3	0.557	0.270	36.977	0.336	
	Sextet-F	Fe^{3+}	40.1	0.334	−0.186	39.729	0.686	
	Doublet	Fe^{2+}	0.8	1.420	2.931	–	0.405	
1.2	Sextet-A	Fe^{3+}	6.9	0.392	0.137	51.826	0.303	1.84
	Sextet-B	Fe^{3+}	16.7	0.443	0.201	49.779	0.498	
	Sextet-C	Fe^{3+}	24.3	0.223	0.014	48.942	0.459	
	Sextet-D	Fe^{3+}	15.5	0.352	0.409	41.009	0.336	
	Sextet-E	Fe^{3+}	10.3	0.595	0.854	38.959	0.546	
	Sextet-F	Fe^{3+}	25.2	0.318	−0.192	39.391	0.638	
	Doublet	Fe^{2+}	1.1	1.614	3.028	–	0.673	
1.6	Sextet-A	Fe^{3+}	6.1	0.379	0.260	51.480	0.211	1.64
	Sextet-B	Fe^{3+}	16.0	0.459	0.246	49.574	0.484	
	Sextet-C	Fe^{3+}	22.1	0.210	0.072	48.759	0.435	
	Sextet-D	Fe^{3+}	22.9	0.348	0.389	41.156	0.390	
	Sextet-E	Fe^{3+}	17.8	0.567	0.890	38.784	0.645	
	Sextet-F	Fe^{3+}	13.9	0.280	−0.110	38.672	0.489	
	Doublet	Fe^{2+}	1.2	1.549	2.835	–	0.395	
2.0	Sextet-A	Fe^{3+}	9.6	0.371	0.272	51.284	0.285	1.56
	Sextet-B	Fe^{3+}	11.6	0.454	0.275	49.191	0.421	
	Sextet-C	Fe^{3+}	22.2	0.221	0.081	48.579	0.408	

Table 6 (*continued*)

Ga-content (x)	Iron sites	Ionic state (high spin)	Relative area (R_A) (%)	Isomer shift* (δ) mm/s ±0.01	Quadrupole splitting (Δ) mm/s ±0.02	Hyperfine field (H_{hf}) Tesla ±0.1	Outer line width (Γ) mm/s ±0.05	Fitting quality (χ^2)
	Sextet-D	Fe^{3+}	21.5	0.348	0.379	40.971	0.346	
	Sextet-E	Fe^{3+}	19.3	0.544	0.968	38.742	0.554	
	Sextet-F	Fe^{3+}	14.5	0.210	−0.031	38.548	0.472	
	Doublet	Fe^{2+}	1.3	1.566	2.715	–	0.460	

exceed it. All samples are also still very soft ferrites, even at 5 K.

In addition to hysteresis, zero-field cooled (ZFC) and field cooled (FC) magnetisationcurves were recorded at an applied magnetic field of 100 Oe for $Sr_3Co_{2-x}Ga_xFe_{24}O_{41}$ (x = 0.0, 0.4, 1.6, and 2.0), as shown in Fig. 8(a). All curves of ZFC and FC show branching due to magnetic ordering. Due to ***the limitation*** of ***the instrument***, we recorded these data up to 300 K, not beyond the transition temperature of samples. For x = 0.0 and 0.4, a clear change in the magnetic ordering was observed at around 140 K, an effect that became less apparent with further levels of substitution. This suggests that Ga substitution for Co reduces the creation of this second lower temperature magnetic phase. For selected compositions of $Sr_3Co_{2-x}Ga_xFe_{24}O_{41}$ (0.4 and 1.6), ZFC and FC curves were further recorded at a higher applied magnetic field of 1000 Oe as shown in Fig. 8(b) showed similar behaviour, the only difference being that the difference between the ZFC and FC branch was reduced, as expected.

3.5.2. Mössbauer analysis

Ina previous report on the Mössbauer analysis of $SrFe_{12-x}M_xO_{19}$ (M = Ga, In, Sc), it was found that the predominant 12k sublattice exhibits a remarkable splitting into two distinct subpatterns, 12k_1 and 12k_2. The 12k_1 hyperfine field values are virtually unchanged from that of the pure hexagonal ferrites and are independent of substitution level. Contrastingly, the abruptness of the drop in the 12k_2 hyperfine field and its dependence on the nature of the substituting cation is remarkable. The relative intensity of the 12k_2 component correlates with the concentration of nonmagnetic species on the 2b and 4f_2 sites and with the magnetic anisotropy. Scandium seems to have a more profound influence on the magnetic structure and interactions than indium or gallium. Further, at technically significant substitution levels, H_{eff} of the different sublattices exhibit broad and overlapping distributions of values far removed from their distinctiveness in the pure hexaferrites. Thus, the net magnetisation of Ga, Sc, and In-doped hexaferrites results from a complex interplay of magnetic dilution on the 2b site, enhancement of the magnetisation through substitutions on the 4f_2 site, and a complex influence from the substitution-induced 12k_2 sublattice [83].

The Mössbauer effect is widely used to study ferrites in order to get fruitful information about the molecular structure and chemical bonding in these materials, and Mössbauer spectra give information on the various co-ordinations that the iron ions occupy on different crystallographic sites. Mössbauer spectra of all compositions were fitted well with six sextets (Zeeman splitting patterns) and a paramagnetic doublet. The analysis results for the $Sr_3Co_{2-x}Ga_xFe_{24}O_{41}$ hexaferrite samples heated at 1200 °C for 5 h are shown in Table 6, and the corresponding Mössbauer spectra are shown in Fig. 9. All six sextets corresponding to the ten crystallographic sites are shown in Table 7 [84]. The assignment of these sextets has been based on the previous work by Li et al. and Kikuchi et al. [61,85].The variations in different parameters with increasing Ga-substitution are shown in Fig. 10(a–h).

Fig. 10(a–d) shows the variation in different parameters with Ga substitution (x) such as relative area (%), isomer shift, quadrupole splitting and hyperfine magnetic field, and Fig. 10(e–h) shows the compositional dependence of relative area of doublet, average hyperfine magnetic field (<H_{hf}>), average quadrupole splitting (<Δ>), and average isomer shift (<δ>) of sextets with Ga substitution (x). The crystal structures were identified to be hexagonal having space

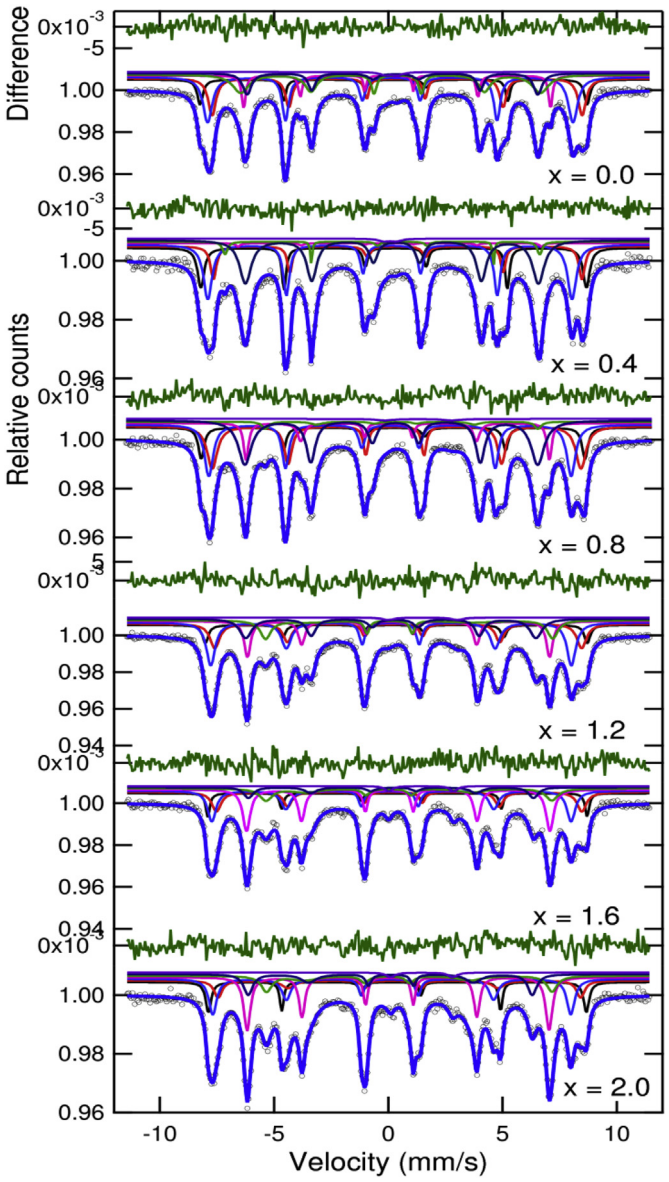

Fig. 9. Room temperature Mössbauer spectra of $Sr_3Co_{2-x}Ga_xFe_{24}O_{41}$ (x = 0.0, 0.4, 0.8, 1.2, 1.6, and 2.0) hexaferrite samples heated at 1200 °C for 5h.

group $P6_3/mmc$. The Fe, Co, and Ga ions were found to be located at six-octahedral sites ($12k_{VI}$, $4f_{VI}$, $4e_{VI}$, $4f_{VI}^*$, $12k_{VI}^*$, and $2a_{VI}$), three tetrahedral sites ($4e_{IV}$, $4f_{IV}$ and $4f_{IV}^*$), and a five-fold site of $2d_V$ [62].

The values of isomer shift for all sextets are found to be between 0.16 and 0.59 mm/s (Table 7 and Fig. 10 b), which depicts that all six sextets are due to Fe^{3+} ions in high spin states [86–89]. The values of isomer shift for doublets in samples with composition $x = 0.8$, 1.2, 1.6 and 2.0 are found to be between 1.4 and 1.6 mm/s. These values relate to Fe^{2+} ions in high spin state at octahedral sites [89–92]. The isomer shift values of the doublet in samples $x = 0.0$ and 0.4 compositions are found to be 0.24 and 0.19, respectively. There was a slight decrease in the hyperfine field for sextets A, B, C, D, and F with Ga substitution. The value H_{hf} in $x = 0.4$ substitution is found to be increased for sextet E and then it decreases at $x = 0.8$ and further increases at $x = 1.2$ and then remains almost constant in samples $x = 1.6$ and $x = 2.0$.The average value of the isomer shift is found to be minimum for the sample with $x = 0.4$ composition [Fig. 11 (h)], which means that the electric monopole interaction is minimum for this sample.

The average value of H_{hf} shows a decreasing trend with Ga substitution [Fig. 10 (f)]. This decreasing trend explains the exchange interactions. Hyperfine field decreases due to the weak interaction among the magnetic and nonmagnetic ions in sublattices. In hexaferrites, the magnetic properties are based on the strength of super-exchange interaction between magnetic and magnetic/nonmagnetic ions. The Fe^{3+} ions reside in the tetrahedral and octahedral sites, which results in strong super-exchange interactions between the Fe^{3+} ions residing in both the sites. The super-exchange interaction between Fe^{3+}-O-Co^{2+}ions is higher than that of Fe^{3+}-O-Ga^{3+} ions. The gallium ions are non-magnetic and so they do not possess a nuclear magnetic field. The introduction of Ga^{3+}(magnetic moment = 0 μ_B) ions in hexaferrite results in the dilution of the magnetisation at the tetrahedral and octahedral sites; which will reduce the saturation magnetisation, and also decrease the hyperfine magnetic fields and saturation magnetisation [Figs. 10 (f) and 6 (c)]. The relative areas of sextets A and C (spin-down) are decreasing with Ga-substitution [Fig. 10 (a)]. This means that the Ga^{3+} ions occupy the spin down sub lattices at these sites, but a drastic decrease in the relative area was observed for sextet F (spin-up), which belongs to the $12k_{VI}$ site, confirmed from the value of isomer shift and hyperfine magnetic field. The area of doublet also increases with Ga-substitution. These aspects also account for the decrease in M_S and H_{hf} with Ga-substitution.

The average value of quadrupole splitting ($< \Delta >$) (Fig. 10 g) is found to be increased with Ga-substitution except forx = 0.4 composition. This increasing trend of quadrupole splitting is attributed to the increase in structural and magnetic distortion with Ga-substitution. The increasingly positive value of Δ indicates that the magnetic anisotropy of $Sr_3Co_{2-x}Ga_xFe_{24}O_{41}$hexaferrites is progressing towards the *c*-axis with substitution [62,87], meaning that the angle of the cone of magnetisation to the c-axis found in unsubstituted SrZ will probably becoming smaller, and H_C will also increase as a result.

3.6. Low frequency dielectric measurements (100 Hz-2 MHz)

The dielectric property is a very significant feature of hexaferrites; which represents the storage of electrical charge in the dielectric material, and it considerably depends on the method of preparation, good selection of materials and heating temperature [93,94]. The variations of real dielectric constant (ε') and dielectric loss tangent (tan δ) with a frequency range of 100 Hz to 2 MHz at room temperature for all samples are shown in Fig. 11 (a) and (b), respectively. The dielectric constant decreases quickly at the lower frequencies, and then proceeds to frequency-independent behaviour at frequencies above ~10 kHz.

The values of the dielectric constant are higher at a lower frequency because the penetration depth of electromagnetic waves is less due to the skin effect [95]. This high values of (ε') are due to the presence of Fe^{2+} ions, interfacial dislocations, grain boundary defects, voids and oxygen vacancies [96,97]. The dielectric constant of any material is directly related to its polarisation. The higher values of polarisation lead to the higher dielectric constant of the material [98]. Various types of polarisation such as ionic, electronic, interfacial, dipolar, etc., contribute to dielectric constant [99]. The observed dielectric behaviour of these samples can be explained using the Maxwell-Wagner interfacial polarisation model, which is in good agreement with Koop's phenomenological model [100,101].These models explain that the dielectric structure consists of fairly well-conducting grains, which are detached by the highly resistive grain boundaries of poorly conducting substances. These grain boundaries are formed during the heat treatment, as a result of the oxidation or reduction of crystallites in the porous materials in consequence of their direct contact with the firing atmosphere [102]. On applying an electric field, the charge carriers are displaced. They align at grain boundaries when the resistance of grain boundaries is large. Hence, there is an increase in space charge polarisation at the grain boundary, which leads to a large dielectric constant. At low frequency, grain boundaries are more effective, while at high frequency, grains are more effective. Therefore, at a higher frequency, the low values of polarisation increase and, as a result, the dielectric constant of the material decreases [103]. On substituting gallium in SrZ hexaferrites, the

Table 7
Coordination, block location, the numbers of ions per formula unit, spin direction and six components (sextets) in Z-Type $Sr_3Co_{2-x}Ga_xFe_{24}O_{41}$ hexaferrite [61,89,90].

Site	Coordination	Block	Number of ions (Fe/Co)	Spin	Components (sextets) in Mössbauer spectrum
$12k_{VI}$	Octahedral	*R–S*	6	up (↑)	E + F
$2d_V$	Fivefold	*R*	1	up (↑)	
$4f_{VI}$	Octahedral	*R*	2	down (↓)	
$4e_{VI}$	Octahedral	*T*	2	down (↓)	A + C
$4e_{IV}$	Tetrahedral	*S*	2	down (↓)	
$4f_{IV}$	Tetrahedral	*S*	2	down (↓)	
$4f^*_{IV}$	Tetrahedral	*T*	2	down (↓)	
$4f^*_{VI}$	Octahedral	*S*	2	up (↑)	B + D
$12k^*_{VI}$	Octahedral	*T-S*	6	up (↑)	
$2a_{VI}$	Octahedral	*T*	1	up (↑)	

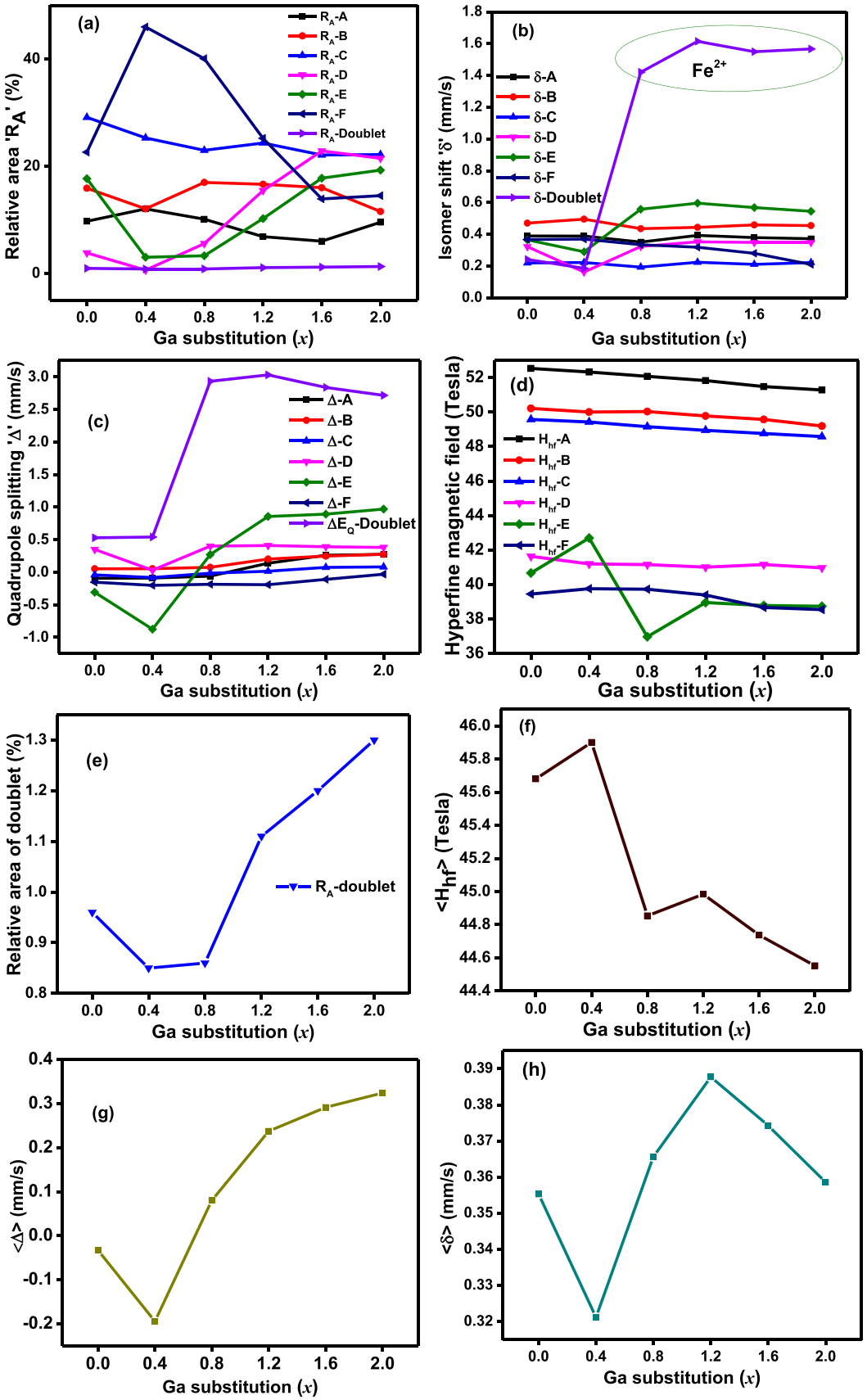

Fig. 10. Variation in (a) relative area (%), (b) isomer shift, (c) quadrupole splitting and(d) hyperfine magnetic field with Ga substitution (x). Compositional dependence of (e) relative area of doublet, (f) average hyperfine magnetic field (<H_{hf}>), (g) average quadrupole splitting (<Δ>), and (h) average isomer shift (<δ>) of sextetsis observed with Ga substitution (x).

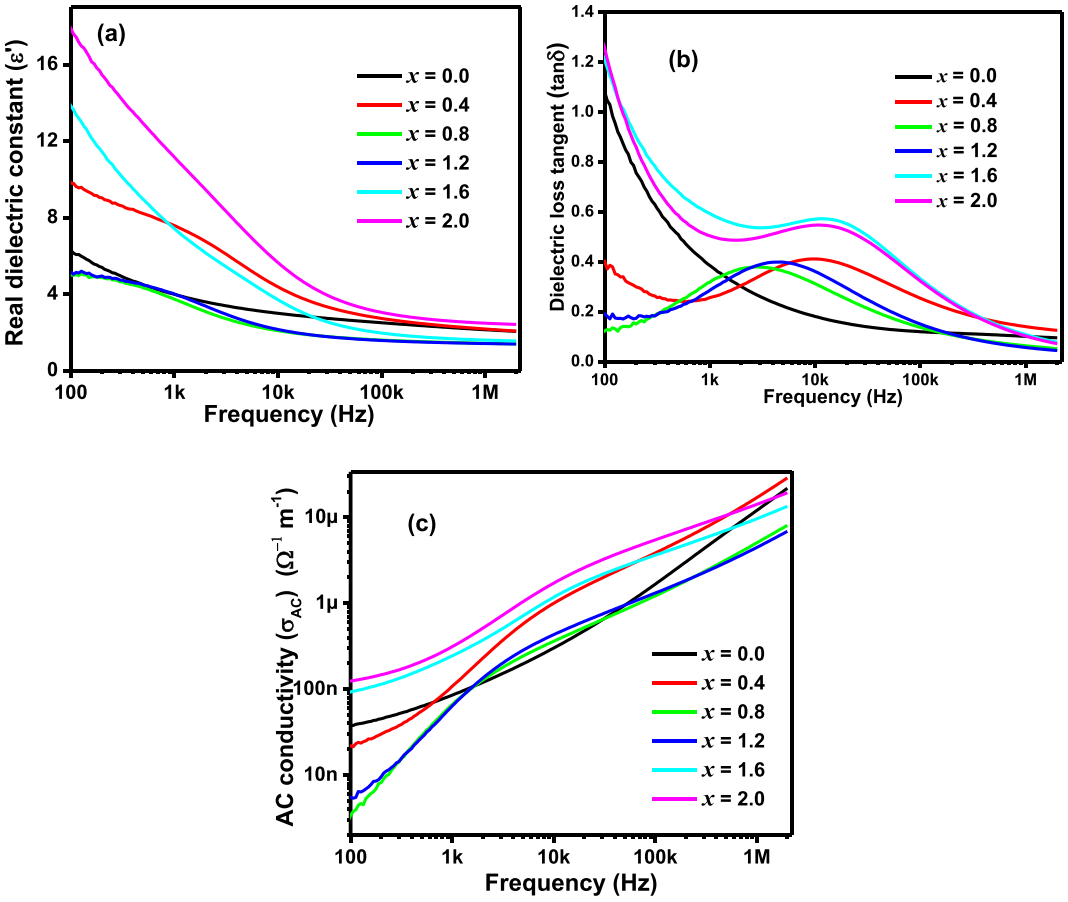

Fig. 11. Variation of (a) real dielectric constant (ε'), (b) dielectric loss tangent (tan δ) and(*c*)AC conductivity (σ_{AC}) as a function of frequency for $Sr_3Co_{2-x}Ga_xFe_{24}O_{41}$ (x = 0.0, 0.4, 0.8, 1.2, 1.6 and 2.0) hexaferrites samples heated at 1200 °C for 5 h.

values of dielectric constant were found to increase initially from ~ 44.73 for $x = 0.0$ to 70.45 for $x = 0.4$, followed by a sudden drop to ~35.89 for $x = 0.8$, and then it drastically increases with higher gallium substitution, i.e. from around 37.00 for $x = 1.2$ to 99.66 for $x = 1.6$ and to 130.40 for $x = 2.0$. The value of the dielectric constant of the fully substituted sample $x = 2.0$ ($Sr_3Ga_2Fe_{24}O_{41}$) is higher compared to other samples. The samples $x = 1.6$ and $x = 2.0$ possess lower bulk density, higher porosity, lower M_S and greater M_r and H_C values.

The dielectric loss tangent (tan δ) is acquired by the ratio of imaginary dielectric constant (ε'') to the real dielectric constant (ε'), and is responsible for the entire core loss. Little core loss leads to little dielectric losses [104]. The values of dielectric loss factors depend on various aspects such as stoichiometry, preparation method, the density of charge carriers, structural homogeneity, and heating temperature [105]. When the applied field is increased, a state is attained where no more charge carriers of dielectric material align in the direction of the applied field. At higher frequencies, polarisation lags behind the applied electric field. The friction produced in the dielectric material resists the dipole motion which results in power loss [106]. The value of dielectric loss factor decreases with an increase in frequency except $x = 0.8$ and $x = 1.2$ which initially increases and then decreases. The sample $x = 0.8$ reveals the minimum loss tangent at lower frequencies. The maximum loss occurs when the hopping frequency is approximately equal to the externally applied field [107]. All samples, except $x = 0.0$ show dielectric relaxation peaks between 5 KHz and 30 KHz frequency.

Fig. 11(c) shows the variation of AC conductivity as a function of frequency from 100 Hz to 2 MHz at room temperature. The AC conductivity of all samples is enhanced with an increase in frequency. Conduction results from the hopping of small polarons

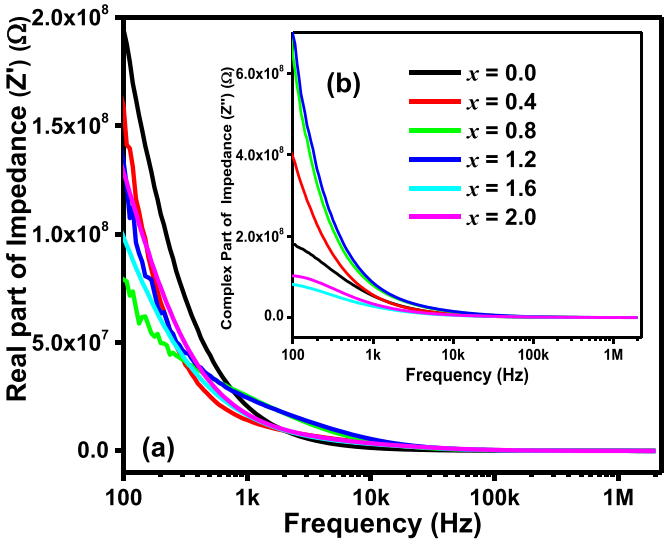

Fig. 12. (a, b).Variation of real dielectric Impedance (Z′) and complex dielectric Impedance (Z″) with frequency of $Sr_3Co_{2-x}Ga_xFe_{24}O_{41}$ (x = 0.0, 0.4, 0.8, 1.2, 1.6, and 2.0) hexaferrite samples heated at 1200 °C for 5h.

within the localised states. In the ionic lattice, similar types of cation are present in two oxidation states (Fe^{3+} and Fe^{2+}), and so electron hopping occurs in the ionic lattice [108]. The approach for small polaron conduction is accurate for ionic solids also. The conduction in ferrites is attributed to the hopping of charges, which results in linearity between angular frequency and AC conductivity. The electrical conductivity occurs due to the migration of ions, which depends on the frequency.

Therefore, the AC conductivity is directly proportional tothe angular frequency [109]. In large polaron model, AC conductivity decreases as frequency increases, while AC conductivity increases with an applied frequency in small polaron model [110]. The samples in the present study show linear behaviour at high frequency, which confirms that the conduction is due to small polaron hopping in all samples. The fully substituted sample is found to be more conducting as compared to other samples, and indeed it possess more Fe^{2+}. The samples with low lattice constants have high conductivity.

3.7. Frequency dependence impedance (100 Hz -2 MHz)

Impedance spectroscopy is one of the important measurements, which is used to get a thorough knowledge about the resistive and reactive components that are real and imaginary part respectively. Fig. 12 (a, b) represents the variation of real dielectric impedance (Z') and complex dielectric impedance (Z'') with frequency respectively. Impedance results of all the **g**allium substituted samples show the normal behaviour. Real dielectric impedance decreases with increasing **g**allium content at low frequencies but remains almost constant for all samples at frequencies beyond 20 kHz.

3.8. Electric modulus analysis (100 Hz - 2 MHz)

The analysis of electric modulus (M) is essential to examine the efficient characteristics of the electrical transference mechanism, which relates to conductivity relaxation time, ions hopping rate etc. The electric modulus analysis is used to study the relaxation behaviour and grain-boundary contribution to the total conductivity of material [111]. It also represents the electrical response of the materials. Electric modulus also suggests the polycrystalline nature, i.e. homogeneous or inhomogeneous [112–114].

The variation of the real part of the electric modulus (M') with the frequency is shown in Fig. 13 (a). It is clearly seen from Fig. 13 (a) that M' in the lower frequency region increased gradually as frequency increases, and reached a maximum at 2 MHz.

This increase in the real part of electric modulus is due to the decrease in restoring force regulating the mobility of charge carriers under the influence of the externally applied electric field. The lack of restoring force indulges the conduction mechanism in hexaferrites, which enhances the conductivity at higher frequencies [115]. Fig. 13 (b) shows the variation of the imaginary part

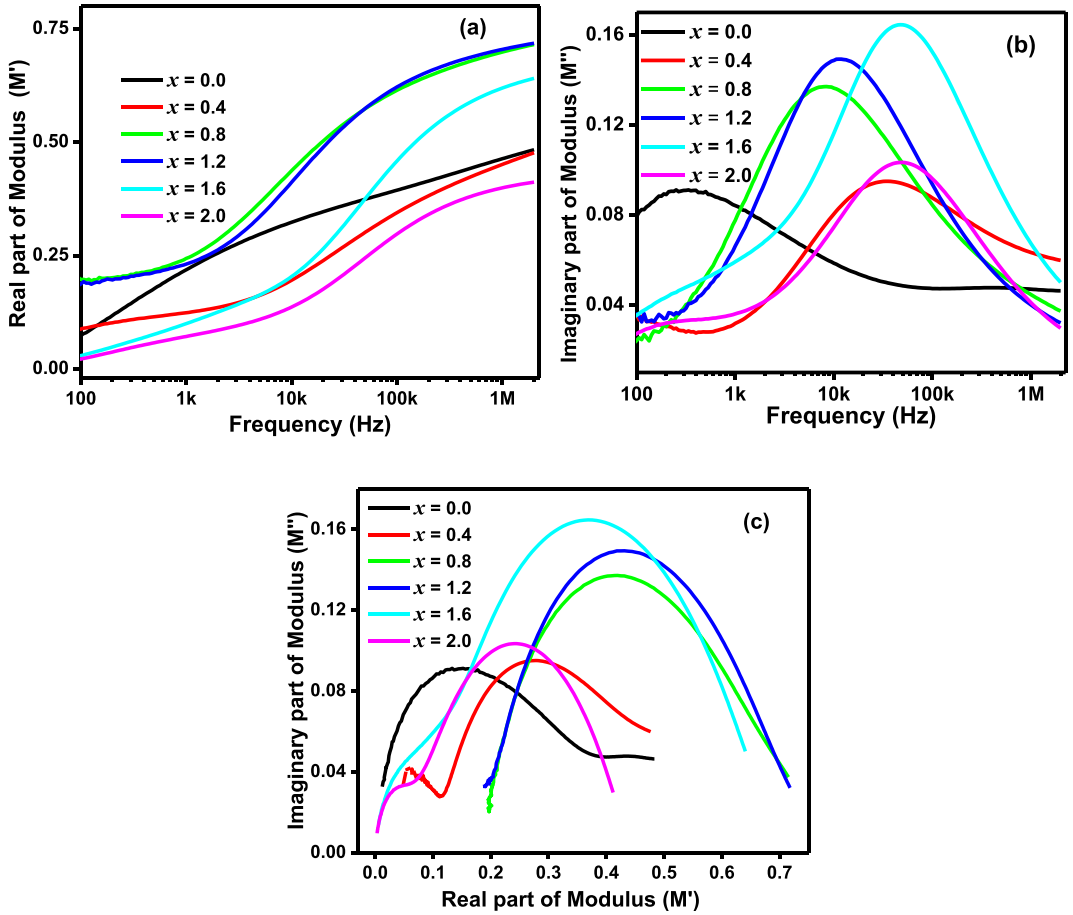

Fig. 13. Variation of (a) Real part of dielectric modulus (M'), (b) Imaginary part of dielectric modulus (M'') with frequency and(c)Cole-Cole type plot of $Sr_3Co_{2-x}Ga_xFe_{24}O_{41}$ (x = 0.0, 0.4, 0.8, 1.2, 1.6 and 2.0) hexaferrite samples heated at 1200 °C for 5h.

of the electric modulus (M'') with frequency. The broad peak observed in all samples exhibits the relaxation peaks for hexaferrites [116].

The frequencies exhibiting maximum peak brings the charge carriers in motion. The charge carriers stop moving beyond the maximum peaks frequencies [117]. As frequency increases, the peaking nature appears; which is due to the transition takes place from long-range to short-range mobility of charge carrier. The response of modulus shows the hopping type mechanism for charge transport in the system. The frequency of the peaks evaluates the conduction relaxation time. The modulus pattern indicates the feasibility of long-range mobility of charge carriers by a hopping mechanism. The peaks of the substituted samples ($x > 0.0$) are shifted in the forward direction compared to pure sample ($x = 0.0$) [118]. The low-frequency side of the peak depicts the range, where charge carriers occur due to long-range hopping. The high-frequency side of the peak signifies the carriers being constrained to potential wells and the electrons are mobile within a short-range distance through the well. The region in which the peak appears shows the transition from long range to short-range mobility with an increase in frequency. This peak occurrence in the modulus response indicates a clear signal for conductivity relaxation [119].

The complex modulus plots known as Cole-Cole plots have been studied to isolate the grains and the grain boundaries contribution. In the Cole-Cole plots, the grains and grain boundary including grain-electrode effects occur as semicircles; which depicts a possible link between behaviour of grain boundaries and peak occurrence in complex modulus (M'' vs F) with the function of frequency [120].

Fig. 13 (c) represents the Cole-Cole type plots of all the heated samples. The samples $x = 0.4$, $x = 1.6$, and $x = 2.0$ show two semicircular arcs; one in the high-frequency region and other in the low-frequency region, correlating to grain and grain boundary resistance, respectively [121,122]. The samples $x = 0.0$, 0.8, 1.2 and 2.0 show single semicircles. The left portion of the semicircles at the lower frequencies is attributed to the grain resistance [118], while the intermediate frequencies over which the curve occurs show grain boundary contribution, and the utmost right side of the curve at high frequencies shows the effect of grain and grain boundaries [123]. The radius of the semicircles in all samples varies, with $x = 0.8$, 1.2 and 1.6 exhibiting the widest curves. Similar effects have been seen in rare-earth substituted ferrites [124].

3.9. Complex permittivity of $Sr_3Co_{2-x}Ga_xFe_{24}O_{41}$ ($x = 0.0$ to 2.0) ferrites at high frequency over the X-band (8 GHz -12.5 GHz)

The material's dynamic properties are studied by complex permittivity and permeability measurements. Complex permittivity represents electronic properties and complex permeability represents magnetic properties when subjected to an electromagnetic field. The real part of complex permittivity (ε') and complex permeability (μ') determine the storage capacity of electric and magnetic energy; while the imaginary part of (ε'') and (μ'') represents the loss of electric and magnetic energies. These parameters combine to describe the lossy behaviour of the material when electromagnetic waves are passed through it [125,126]. The complex permittivity of hexaferrites is usually linked with ionic, electronic and interfacial polarisations [127].

The variation of real (ε') and imaginary (ε'') permittivity of the $Sr_3Co_{2-x}Ga_xFe_{24}O_{41}$ ($x = 0.0$, 0.4, 1.2, 1.6 and 2.0) ferrites with

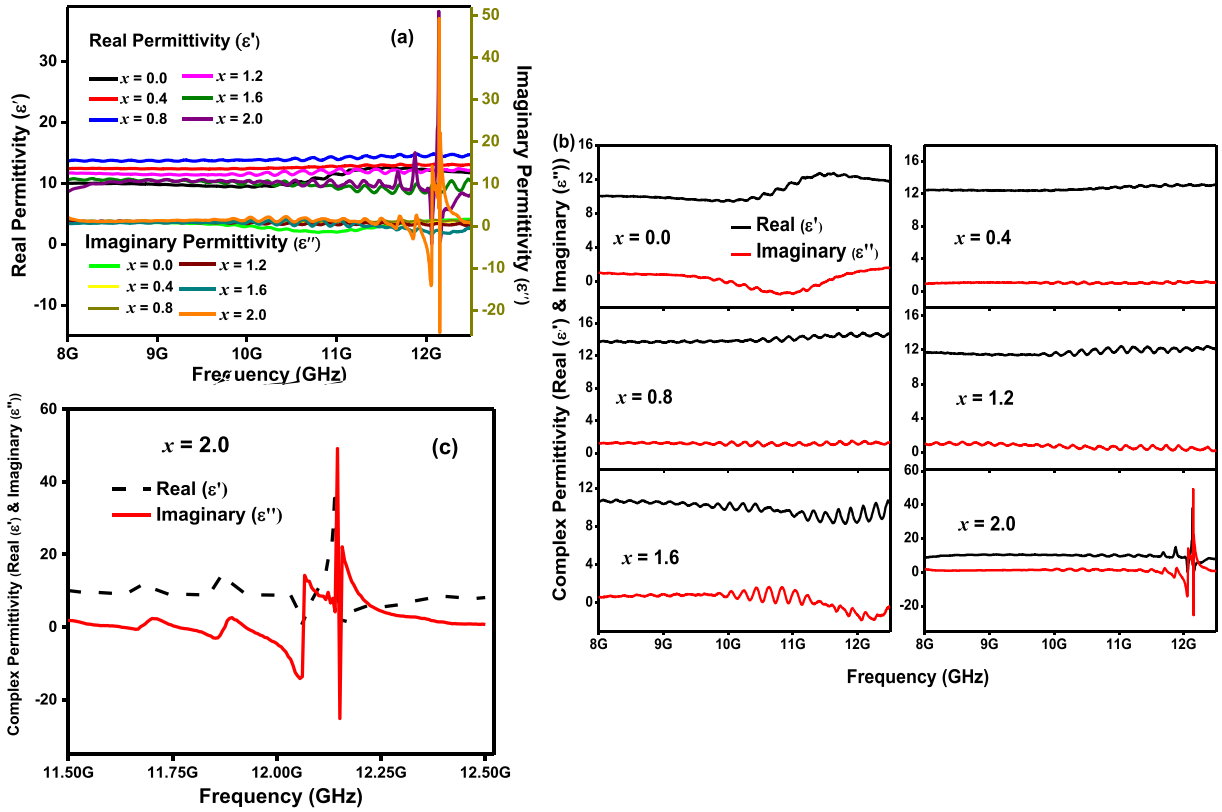

Fig. 14. (a) Variation of real (ε') and complex permittivity (ε'') with the frequency between 8 GHz and 12.5 GHz, (b) Complex permittivity (Real and imaginary) plots and, (c) Changes in real and complex permittivity with frequency from 11.50 GHz to 12.50 GHz for $x = 2.0$ sample heated at 1200 °C for 5h.

frequency of 8 GHz −12.5 GHz is shown in Fig. 14 (a). All samples have a real permittivity (ε′) around 8−14. Fig. 14 (b) shows the individual complex permittivity plots for $x = 0.0$ to 2.0. Resonance takes place when a peak in the imaginary coincides with the halfway point in a drop of the real for either permeability or permittivity. It can be seen from Fig. 14 (b) that only $x = 2.0$ shows a resonance in the real and imaginary part of permittivity with maximum values of 38.23 and 49.19 at ~12.15 GHz (Fig. 14 (c)).

3.10. Complex permeability measurements at high frequency over the X-band (8 GHz −12.50 GHz)

Fig. 15 (a) shows the variation of complex permeability (real (μ′) and imaginary (μ")) of the $Sr_3Co_{2-x}Ga_xFe_{24}O_{41}$ ferrites between 8 GHz and 12.50 GHz.

The real permeability (μ′) values of all samples are around 1.0−1.4 over the 8−12.5 GHz range. The maximum value of μ′ obtained at the lowest frequency is ~1.4 for the sample with $x = 0.0$. Ferromagnetic resonance (FMR) is the resonance in the complex permeability. At this frequency, energy is absorbed and so such materials are important as EM absorbers and shields, radar absorbing materials (RAM) and stealth technology [9]. The sample with $x = 2.0$ shows a resonance at around 12.15 GHz, and $x = 0.0$ showed a FMR at around 11 GHz (Fig. 15(b)). This suggests that such materials can be used as microwave absorbers/EMI shielding at specific microwave frequencies. That fact that $x = 2.0$ had both FMR and dielectric resonance at the same frequency, 12.15 GHz, suggests the possibility of coupling these two properties, and the

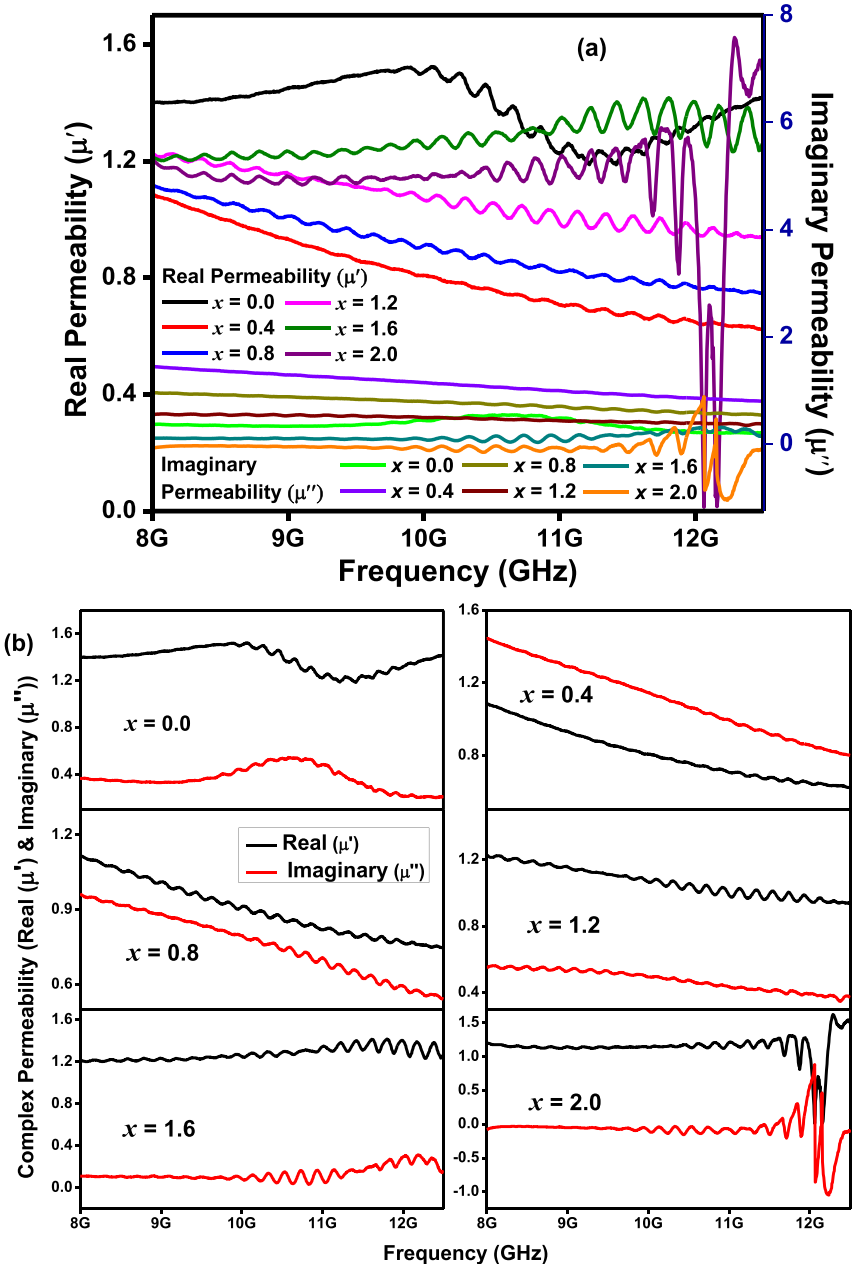

Fig. 15. (a) Variation of complex permeability (μ′) and (μ") with the frequency between 8 GHz and 12.50 GHz and (b) Complex permeability (Real and imaginary) plots of $Sr_3Co_{2-x}Ga_xFe_{24}O_{41}$ ($x = 0.0$, 0.4, 1.2, 1.6 and 2.0) hexaferrites heated at 1200 °C for 5h.

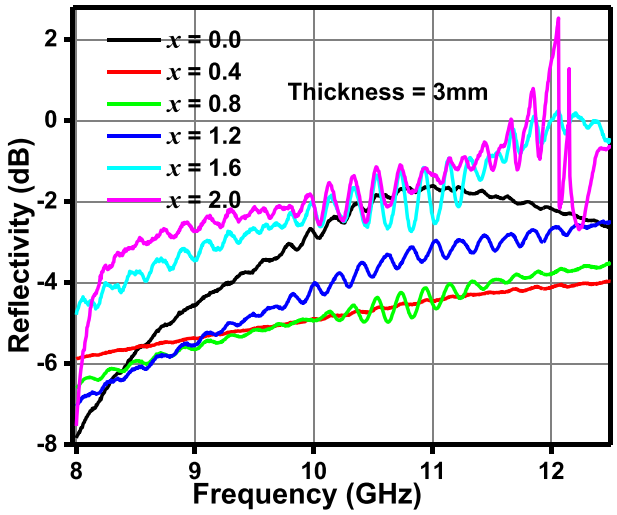

Fig. 16. Reflectivity curves of $Sr_3Co_{2-x}Ga_xFe_{24}O_{41}$ (x = 0.0, 0.4, 0.8, 1.2, 1.6 and 2.0) hexaferrite 3 mm thick samples heated at 1200 °C for 5h.

development of metamaterials.

Fig. 16 represents the variation of reflectivity as a function of frequency of $Sr_3Co_{2-x}Ga_xFe_{24}O_{41}$ (x = 0.0, 0.4, 0.8, 1.2, 1.6 and 2.0) hexaferrite samples heated at 1200 °C for 5 h and of 3 mm thickness. It is clear from Fig. 16 that reflectivity varies from −8 dB to 2.3 dB (thickness 3 mm) for all samples.

4. Conclusions

Ga substituted Z-type $Sr_3Co_{2-x}Ga_xFe_{24}O_{41}$ (x = 0.0, 0.4, 0.8, 1.2, 1.6 and 2.0) hexaferrites were successfully synthesised using the sol-gel auto-combustion method. XRD analysis reveals the formation of Z-phase along with W, Y and M phases. Prepared Sr-Z hexaferrites exhibited typical soft magnetic behaviour. The saturation magnetisation lies in the range of 64–76 Am^2kg^{-1}. Substitution of gallium led to a decrease in saturation magnetisation values. The decrease in M_S with Ga substitution is well matched by Mössbauer spectroscopic analysis, as the hyperfine magnetic field of all sextets was found to be decreased and the relative area of the doublet is found to increase with Gallium substitution. Mössbauer spectroscopic analysis also confirmed that the Fe ions were found in the 3 + high spin state for compositions below $x \leq 0.4$, whereas ~1.5% of the Fe ions were converted into Fe^{2+} high spin state beyond $x \geq 0.8$ compositions, as Ga^{3+} began to substitute for Fe^{3+}, instead of Co^{2+}, forming Fe^{2+} in the cobalt positions. The low-frequency dielectric response of prepared samples shows normal behaviour and is explained by Maxwell-Wagner's model. At Microwave frequencies (8 GHz–12.50 GHz), all samples showed real permittivity around 8–14. Dielectric resonance observed at around 12.15 GHz in $x = 2.0$. Real permeability was found around 1.0–1.4 over the 8 GHz–12.50 GHz range, and ferromagnetic resonance was observed at around 11 GHz for $x = 0.0$ and 12.15 GHz for $x = 2.0$, and hence such materials could be used as microwave absorbers/EMI shielding at specific microwave frequencies. The reflectivity varies from −8 dB to 2.3 dB for thickness 3 mm in all samples over the X-band. That fact that $x = 2.0$ had both FMR and dielectric resonance at the same frequency, 12.15 GHz, suggests the possibility of coupling these two properties, and the development of metamaterials.

Author contribution

Preksha N: Dhruv. Prepared samples, data analysis, low frequency measurements, FTIR measurements, preparing graphs, writing manuscript. Sher Singh Meena, Pramod bhatt: Mössbauer data recording and Analysis, Rietveld refinement of xrd. Robert C. Pullar: XRD, VSM measurements, over all manuscript checking, analysis, revision, modifications. Francisco E. Carvalho: High frequency measurements and analysis. C. L. Prajapat and T. V. C. Rao: Hysteresis loops and FC-ZFC measurements. Rajshree B Jotania: Defining problem, selection of series with composition, compiling manuscript, checking manuscript, looking over all progress time to time, corresponding author, Research guide. João Paulo Barros Machado: FE-SEM measurements. C. B. Basak: SEM image recording.

Declaration of interest

The authors declare that they have not known to competing financial interest or personal relationship that could appeared to influence to work reported to this paper.

Acknowledgements

This work was supported by DRS-SAP (Phase-II,F-530/17/DRS-II/2018 (SAP-I)) grant of UGC, New Delhi, India and DST-FIST((level- I, No. SR/FST/PSI-198/2014)) grant of Department of science and technology, India. This work was developed within the scope of the project CICECO-Aveiro Institute of Materials, FCT (Fundaçãopara a Ciênciae a Tecnologia, Portugal) Ref. UID/CTM/50011/2019, financed by national funds through the FCT/MCTES, and R.C. Pullar thanks FCT grant IF/00681/2015 for supporting this work.

Appendix A. Supplementary data

Supplementary data to this article can be found online at https://doi.org/10.1016/j.jallcom.2019.153470.

References

[1] I.V. Zavislyak, M.A. Popov, G. Srinivasan, A cut-off millimeter wave resonator technique for mapping magnetic parameters in hexagonal ferrites, Meas. Sci. Technol. 20 (2009) 115704–115708.
[2] M.K. Tehrani, A. Ghasemi, R.S. Alam, Wideband electromagnetic wave absorber using doped barium hexaferrite in Ku-band, J. Alloy. Comp. 509 (2011) 8398–8400.
[3] C.L. Dube, S.C. Kashyap, R. Kotnala, Effect of microwave processing on polycrystalline hard barium hexaferrite, J. Supercond. Nov. Magnetism 24 (2011) 567–570.
[4] Y. Feng, T. Qiu, C. Shen, Absorbing properties and structural design of microwave absorbers based on carbonyl iron and barium ferrite, J. Magn. Magn. Mater. 318 (2007) 8–13.
[5] C.J. Li, B. Wang, J.N. Wang, Magnetic and microwave absorbing properties of electrospun $Ba_{(1-x)}La_xFe_{12}O_{19}$ nanofibers, J. Magn. Magn. Mater. 324 (2012) 1305–1311.
[6] C.J.V. Klemperer, D. Maharaj, Composite electromagnetic interference shielding materials for aerospace applications, Compos. Struct. 91 (2009) 467–472.
[7] J. Smit, H.P.J. Wijn, In Ferrites, Philips Technical Library, Eindhoven, 1959, p. 257.
[8] P.B. Braun, The crystal structures of a new group of ferromagnetic compounds, Phillips Res. Rep. 12 (1957) 491–548.
[9] R.C. Pullar, Hexagonal ferrites: a review of the synthesis, properties and applications of hexaferrite ceramics, Prog. Mater. Sci. 57 (2012) 1191–1334.
[10] Y. Takada, T. Nakagawa, M. Tokunaga, Y. Fukuta, T. Tanaka, T.A. Yamamoto, Crystal and magnetic structures and their temperature dependence of Co_2Z-type hexaferrite $(Ba,Sr)_3Co_2Fe_{24}O_{41}$ by high-temperature neutron diffraction, J. Appl. Phys. 100 (1–7) (2006), 043904.
[11] J.H. Hankiewicz, Nuclear magnetic resonance in $Ba_3Co_2Fe_{24}O_{41}$ ferrite, J. Magn. Magn. Mater. 101 (1991) 134–136.
[12] R.C. Pullar, S.G. Appleton, M.H. Stacey, M.D. Taylor, A.K. Bhattacharya, The synthesis and characterisation of aligned fibres of the ferroxplana ferrites

Co_2Z, 0.67% CaO-doped Co_2Z, Co_2Y and Co_2W, J. Magn. Magn. Mater. 186 (1998) 313–325.
[13] S.B.S. Magham, M. Sharma, S.R. Shannigrahi, H.R. Tan, V. Sharma, Yu Song Meng, S. Idapalpati, R.V. Ramanujan, D.V.M. Repaka, Development of Z-type hexaferrites for high frequency EMI shielding applications, J. Magn. Magn. Mater. 441 (2017) 303–309.
[14] S. Jun Hai, C. KeYu, L.L. Chao, D. Yan, L.J. Bi, K. WeiQiu, Fabrication of Z-type barium ferrite/silica composites with enhanced microwave absorption, Sci. China Technol. Sci. 57 (2014) 1858–1864.
[15] R.C. Pullar, A.K. Bhattacharya, The synthesis and characterization of the hexagonal Z ferrite, $Sr_3Co_2Fe_{24}O_{41}$, from a sol–gel precursor, Mater. Res. Bull. 36 (2001) 1531–1538.
[16] Y. Takada, T. Tachibana, T. Nakagawa, T.A. Yamamoto, T. Shimada, S. Kawano, Estimation of magnetic structures of Z-type ferrites: $(Ba, Sr)_3Co_2Fe_{24}O_{41}$ by neutron diffraction, J. Jpn. Soc. Powder Powder Metall. 50 (2003) 618–625.
[17] Y. Kitagawa, Y. Hiraoka, T. Honda, T. Ishikura, H. Nakamura, T. Kimura, Low field magnetoelectric effect at room temperature, Nat. Mater. 9 (2010) 797–802.
[18] M. Soda, T. Ishikura, H. Nakamura, Y. Wakabayashi, Tsuyoshi, magnetic ordering in relation to the room-temperature, magnetoelectric effect of $Sr_3Co_2Fe_{24}O_{41}$, Phys. Rev. Lett. 106 (1–4) (2011), 087201.
[19] X. Wang, Z. Su, A. Sokolov, B. Hu, P. Andalib, Y. Chen, V.G. Harris, Giant magnetoresistance due to magnetoelectric currents in $Sr_3Co_2Fe_{24}O_{41}$ Hexaferrites, Appl. Phys. Lett. 105 (1–4) (2014) 112408.
[20] J. Wu, Z. Shi, J. Xu, N. Li, Z. Zheng, H. Geng, Z. Xie, L. Zheng, Synthesis and room temperature four-state memory prototype of $Sr_3Co_2Fe_{24}O_{41}$ multiferroics, Appl. Phys. Lett. 101 (1–4) (2012) 122903.
[21] K. Ebnabbasi, C. Vittoria, A. Widom, Converse magnetoelectric experiments on a room-temperature spirally ordered hexaferrite, Phys. Rev. B. 86 (1–4) (2012), 024430.
[22] T. Kikuchi, T. Nakamura, T. Yamasaki, M. Nakanishi, T. Fujii, J. Takada, Y. Ikeda, Synthesis of single-phase $Sr_3Co_2Fe_{24}O_{41}$ Z-type ferrite by polymerizable complex method, Mater. Res. Bull. 46 (2011) 1085–1087.
[23] S. Ruan, B. Xu, H. Suo, F. Wu, S. Xiang, M. Zhao, Microwave absorptive behavior of ZnCo-substituted W-type Ba hexaferrite nanocrystalline composite material, J. Magn. Magn. Mater. 212 (1–2) (2000) 175–177.
[24] H. Zhang, J. Zhou, L. Li, Z. Yue, Z. Gui, Dielectric characteristics of novel Z-type planar hexaferrite with Cu modification, Mater. Lett. 55 (2002) 351–356.
[25] T. Koutzarova, S. Kolev, Ch Ghelev, B. Vertruyen, A. Zaleski, Synthesis and Investigation of the Properties of Hexaferrites Obtained by Microemulsion Techniques, Microemulsions: Systems, Properties and Applications Chapter: 2 Publisher, in: Taylor Torres (Ed.), Nova Science Publishers, Inc., 2017, pp. 37–82.
[26] D. Chen, Y. Meng, K.H. Gandha, D. Zeng, H. Yu, P. Liu, Morphology control of hexagonal strontium ferrite micro/nano-crystals, AIP Adv. 7 (2017) 56214–56215.
[27] J. Singh, C. Singh, D. Kaur, H. Zaki, I.A. Abdel-Latif, S. Bindra Narang, R. Jotania, S.R. Mishra, R. Joshi, P. Dhruv, M. Ghimire, S.E. Shirsath, S.S. Meena, Elucidation of phase evolution, microstructural, Mössbauer and magnetic properties of Co^{2+} Al^{3+} doped M-type Ba Sr hexaferrites synthesised by a ceramic method, J. Alloy, Comp 695 (2017) 1112–1121.
[28] D. Chen, D. Zeng, Z. Liu, Synthesis, structure, morphology evolution and magnetic properties of single domain strontium hexaferrite particles, Mater. Res. Express 3 (2016) 45002–45010.
[29] S. Katlakunta, S.S. Meena, S. Srinath, M. Bououdina, R. Sandhya, K. Praveena, Improved magnetic properties of Cr^{3+} doped $SrFe_{12}O_{19}$ synthesised via microwave hydrothermal route, Mater. Res. Bull. 63 (2015) 58–66.
[30] D.Y. Chen, Y.Y. Meng, D.C. Zeng, Z.W. Liu, H.Y. Yu, X.C. Zhong, CTAB-assisted low-temperature synthesis of $SrFe_{12}O_{19}$ ultrathin hexagonal platelets and its formation mechanism, Mater. Lett. 76 (2012) 84–86.
[31] M. Hashim, S.E. Shirsath, S.S. Meena, M.L. Mane, S. Kumar, P. Bhatt, R. Kumar, N.K. Prasad, S.K. Alla, J. Shah, R.K. Kotnala, K.A. Mohammed, E. Senturk, Alimuddin, Manganese ferrite prepared using reverse micelle process: structural and Magnetic properties characterization, J. Alloy. Comp. 642 (2015) 70–77.
[32] P. Kaur, S.K. Chawla, S.S. Meena, S.M. Yusuf, K. Pubby, S. BindraNarang, Modulation of physico-chemical, magnetic, microwave and electromagnetic properties of nanocrystalline strontium hexaferrite by Co-Zr doping using citrate precursor sol- gel method, Ceram. Int. 43 (2017) 590–598.
[33] S.K. Chawla, R.K. Mudsainiyan, S.S. Meena, S.M. Yusuf, Sol-gel synthesis, structural and magnetic properties of nanoscale M-type barium hexaferrites $BaCo_xZr_xFe_{(12-2x)}O_{19}$, J. Magn. Magn. Mater. 350 (2014) 23–29.
[34] L. Kopanja, I. Milosevic, M. Panjan, V. Damnjanovi, M. Tadic, Sol–gel combustion synthesis, particle shape analysis and magnetic properties of hematite (α-Fe_2O_3) nanoparticles embedded in an amorphous silica matrix, Appl. Surf. Sci. 362 (2016) 380–386.
[35] F. Haberey, R. Leckebusch, M. Rosenberg, K. Sahl, Flux growth of $SrGa_{12}O_{19}$ single crystals, J. Cryst. Growth 61 (1983) 284–288.
[36] P. Röschmann, M. Lemke, W. Tolksdorf, F. Welz, Anisotropy fields and FMR linewidth in single-crystal Al, Ga and Sc substituted hexagonal ferrites with M structure, Mater. Res. Bull. 19 (1984) 385–392.
[37] R. Varadinova, V. Nikolova, P. Pesheva, Growth of single crystals of Ga-, Al- or (Mn + Ti)-substituted barium hexaferrite, J. Cryst. Growth (1993) 97–104.
[38] L. Půst, P.E. Wigen, M. Ramesh, P. Široký, K. Suk, Domain wall resonance in Ga substituted magnetoplumbite, J. Magn. Magn. Mater. 54–57 (1986) 1195–1196.
[39] U. Raina, S. Bhat, P.N. Kotru, F. Licci, Evaluation of $SrGa_xInyFe_{12-(x+y)}O_{19}$ single crystals, Mater. Chem. Phys. 39 (1994) 110–117.
[40] G. Albanese, F. Leccabue, B.E. Watts, S. Diaz-Castanon, Magnetic and Mossbauer investigation of $PbFe_{12-x}Ga_xO_{19}$ hexagonal ferrites, J. Mater. Sci. 37 (2002) 3759–3763.
[41] S.V. Trukhanov, A.V. Trukhanov, V.G. Kostishin, L.V. Panina, I.S. Kazakevich, V.A. Turchenko, V.V. Oleinik, E.S. Yakovenko, L.Y. Matsui, Magnetic and absorbing properties of M-type substituted hexaferrites $BaFe_{12-x}Ga_xO_{19}$ ($0.1 < x < 1.2$), J. Exp. Theor. Phys. 123 (2016) 461–469.
[42] A.V. Trukhanov, S.V. Trukhanov, V.A. Turchenko, V.V. Oleinik, E.S. Yakovenko, L.Y. Matsui, L.L. Vovchenko, V.L. Launets, I.S. Kazakevich, S.G. Dzhabarov, Crystal structure, magnetic, and microwave properties of solid solutions $BaFe_{12-x}Ga_xO_{19}$ ($0.1 \leq x \leq 1.2$), Phys. Solid State (2016) 1792–1797.
[43] S.V. Trukhanov, A.V. Trukhanov, V.G. Kostishyn, L.V. Panina, An V. Trukhanov, V.A. Turchenko, D.I. Tishkevich, E.L. Trukhanova, O.S. Yakovenko, L. Yu Matzui, D.A. Vinnik, D.V. Karpinsky, Effect of gallium doping on electromagnetic properties of barium hexaferrite, J. Phys. Chem. Solids 111 (2017) 142–152.
[44] S.V. Trukhanov, A.V. Trukhanov, V.G. Kostishyn, L.V. Panina, An V. Trukhanov, V.A. Turchenko, D.I. Tishkevich, E.L. Trukhanova, V.V. Oleynik, O.S. Yakovenko, L.Yu Matzui, D.A. Vinnik, Magnetic, dielectric and microwave properties of the $BaFe_{12-x}Ga_xO_{19}$ ($x \geq 1.2$) solid solutions at room temperature, J. Magn. Magn. Mater. 442 (2017) 300–310.
[45] A.V. Trukhanov, V.G. Kostishyn, L.V. Panina, S.H. Jabarov, V.V. Korovushkin, S.V. Trukhanov, E.L. Trukhanova, Magnetic properties and Mössbauer study of gallium doped M-type barium hexaferrites, Ceram. Int. 43 (2017) 12822–12827.
[46] A.V. Trukhanov, L.V. Panina, S.V. Trukhanov, V.G. Kostishyn, V.A. Turchenko, D.A. Vinnik, T.I. Zubar, E.S. Yakovenko, L. Yu Macuy, E.L. Trukhanova, Critical influence of different diamagnetic ions on electromagnetic properties of $BaFe_{12}O_{19}$, Ceram. Int. 44 (2018) 13520–13529.
[47] V.A. Turchenko, S.V. Trukhanov, A.M. Balagurov, V.G. Kostishyn, A.V. Trukhanov, L.V. Panina, E.L. Trukhanova, Features of crystal structure and dual ferroic properties of $BaFe_{12-x}Me_xO_{19}$ (Me = In^{3+} and Ga^{3+}; x = 0.1–1.2), J. Magn. Magn. Mater. 464 (2018) 139–147.
[48] S.V. Trukhanov, A.V. Trukhanov, V.G. Kostishyn, N.S. Zabeivorot, L.V. Panina, An V. Trukhanov, V.A. Turchenko, E.L. Trukhanova, V.V. Oleynik, O.S. Yakovenko, L. Yu Matzui, V.E. Zhivulin, High-frequency absorption properties of gallium weakly doped barium hexaferrites, Philos. Mag. 99 (2019) 585–605.
[49] B. Kaur, M. Bhat, F. Licci, R. Kumar, P.N. Kotru, K.K. Bamzai, Effect of 50 MeV Li^{3+} ion irradiation on mechanical characteristics of pure and Ga–In substituted M-type strontium hexaferrite, Nucl. Instrum. Methods Phys. Res. B222 (2004) 175–186.
[50] M.J. Iqbal, M.N. Ashiq, P. Hernandez-Gomez, J.M. Munoz, Synthesis, physical, magnetic and electrical properties of Al–Ga substituted co-precipitated nanocrystalline strontium hexaferrite, J. Magn. Magn. Mater. 320 (2008) 881–886.
[51] I. Bsoul, S.H. Mahmood, Magnetic and structural properties of $BaFe_{12-x}Ga_xO_{19}$ nanoparticles, J. Alloy. Comp. 489 (2010) 110–114.
[52] E.H. Na, J.-H. Lee, S.-J. Ahn, K.-P. Hong, Y.M. Koo, H.M. Jang, Local spin reversal and associated magnetic responses in Ga-substituted Pb-hexaferrites, J. Magn. Magn. Mater. 324 (2012) 2866–2870.
[53] V.G. Kostishin, V.G. Andreev, D.N. Chitanov, A.G. Nalogin, N.D. Ursulyak, A.A. Alekseev, A.V. Timofeev, A. Yu Adamtsev, Effects of base composition and dopants on the properties of hexagonal ferrites, Russ. J. Inorg. Chem. 61 (2016) 279–283.
[54] I. Ali, M. Islam, M. Awan, M. Ahmad, Effects of Ga–Cr substitution on structural and magnetic properties of hexaferrite ($BaFe_{12}O_{19}$) synthesized by sol–gel auto-combustion route, J. Alloy. Comp. 547 (2013) 118–125.
[55] F. Aen, M. Ahmad, M.U. Rana, The role of Ga substitution on magnetic and electromagnetic properties of nano-sized W-type hexagonal ferrites, Curr. Appl. Phys. 13 (2013) 41–46.
[56] S.H. Mahmood, Q. Al Sheyab, I. Bsoul, O. Mohsen, A. Awadallah, Structural and magnetic properties of Ga-substituted Co_2W hexaferrites, Curr. Appl. Phys. 18 (2018) 590–598.
[57] M. Wu, L. Liu, Z. Liu, Investigation on the electric and magnetoelectric properties of $BaSrCo_2Fe_{11.5}Ga_{0.5}O_{22}$ ferrite, J. Mater. Sci. Mater. Electron. 29 (2018) 17865–17871.
[58] M. Rasly, M.M. Rashad, Structural and magnetic properties of Sn–Zn doped $BaCo_2Z$-type hexaferrite powders prepared by citrate precursor method, J. Magn. Magn. Mater. 337–338 (2013) 58–64.
[59] M. Hashim, Alimuddin, S.E. Shirsath, S.S. Meena, R.K. Kotnala, S. Kumar, P. Bhatt, R.B. Jotania, R. Kumar, Study of structural and magnetic properties of (Co-Cu)Fe_2O_4/PANI composites, Mater. Chem. Phys. 141 (2013) 406–415.
[60] M.J. Iqbal, M.N. Ashiq, I.H. Gul, Physical, electrical and dielectric properties of Ca-substituted strontium hexaferrite ($SrFe_{12}O_{19}$) nanoparticles synthesised by co-precipitation method, J. Magn. Magn. Mater. 322 (2010) 1720–1726.
[61] Z.W. Li, Guoqing Lin, Nai-Li Di, Zhao-Hua Cheng, C.K. Ong, Mössbauer spectra of CoZn-substituted Z-type barium ferrite $Ba_3Co_{2-x}Zn_xFe_{24}O_{41}$, Phys. Rev. B. 72 (1–7) (2005) 104420.
[62] J.T. Lim, I. Shim, E. Hahn, C.S. Kim, The crystalline and magnetic properties of Zn doped strontium Z-type hexaferrite synthesized by polymerizable complex method, AIP Adv. 7 (1–6) (2017), 056108.

[63] R.C. Pullar, P. Marques, J. Amaral, J.A. Labrincha, Magnetic wood-based biomorphic $Sr_3Co_2Fe_{24}O_{41}$ Z-type hexaferrite ecoceramics made from cork templates, Mater. Des. 82 (2015) 297–303.

[64] F. Song, X. Shen, J. Xiang, H. Song, Formation and magnetic properties of M-Sr ferrite hollow fibres via organic gel-precursor transformation process, Mater. Chem. Phys. 120 (2010) 213–216.

[65] N. Singh, A. Agarwal, S. Sanghi, P. Singh, Synthesis, microstructure, dielectric and magnetic properties of Cu substituted Ni-Li ferrites, J. Magn. Magn. Mater. 323 (2011) 486–492.

[66] M. Penchal Reddy, I.G. Kim, D.S. Yoo, W. Madhuri, M. Venkata Ramana, A. Shaaban, N. Ramamanohar Reddy, K.V. Siva Kumar, R. Ramakrishna Reddy, Effect of La substitution on structural and magnetic properties of microwave treated $Mg_{0.35}Cu_{0.05}Zn_{0.60}La_xFe_{2x}O_4$ ceramics, Superlattice Microstruct. 56 (2013) 99–106.

[67] S.E. Shirsath, B.G. Toksha, R.H. Kadam, S.M. Patange, D.R. Mane, G.S. Jangam, A. Ghasemi, Doping effect of Mn^{2+} on the magnetic behavior in Ni–Zn ferrite nanoparticles prepared by sol–gel auto-combustion, J. Phys. Chem. Solids 71 (2010) 1669–1675.

[68] B.K. Labde, Madan C. Sable, N.R. Shamkuwar, Structural and infra-red studies of $Ni_{1+x}Pb_xFe_{2x}O_4$ system, Mater. Lett. 57 (11) (2003) 1651–1655.

[69] A. Elahi, M. Ahmad, I. Ali, M. Rana, Preparation and properties of sol–gel synthesized Mgsubstituted Ni2Y hexagonal ferrites, Ceram. Int. 39 (2013) 983–990.

[70] I. Sadiq, S. Naseem, M. Rana, M.N. Ashiq, I. Ali, Temperature dependent magnetic and microwave absorption properties of doubly substituted nanosized material, J. Magn. Magn. Mater. 385 (2015) 236–242.

[71] W. Von Aulock, Handbook of Microwave Ferrite Materials, Academic, New York, 1965, p. 407.

[72] H. Kaur, C. Singh, A. Marwaha, S. BindraNarang, R. Jotania, S.R. Mishra, Y. Bai, K.C. James Raju, D. Singh, Madhav, P. Dhruv, A.S.B. Sombra, Elucidation of microwave absorption mechanisms in Co–Ga substituted Ba–Srhexaferrites in X-band, J. Mater. Sci. Mater. Electron. 29 (2018) 14995–15005.

[73] J.J. Xu, C.M. Yang, H.F. Zou, Y.H. Song, G.M. Gao, B.C. An, S.C. Gan, Electromagnetic and microwave absorbing properties of Co_2Z-type hexaferrites doped with La^{3+}, J. Magn. Magn. Mater. 321 (2009) 3231–3235.

[74] Widyastuti, NiaSasria, A.M. Alviani, R.M. DwiFebri, Vania mitha, Ni and Zn substituted M-type barium hexaferrite processed by sol–gel auto combustion method, J. Phys. Conf. Ser. 877 (2017), 012015.

[75] NiaSasria, H. Ardhyananta, R. Fajarin and Widyastuti, Synthesis and characterization of $BaFe_{12}O_{19}$/Poly(aniline, pyrrole, ethylene terephthalate) composites coatings as radar absorbing material (RAM), I, 2017 , J. Phys. Conf. Ser. 877, 012057.

[76] Y. Kitagawa, Y. Hiraoka, T. Honda, T. Ishikura, H. Nakamura, T. Kimura, Low field magnetoelectric effect at room temperature, Nat. Mater. 9 (2010) 797–802.

[77] M. Ahmad, F. Aen, M.U. Islam, S.B. Niazi, M.U. Rana, Structural, physical, magnetic and electrical properties of La-substituted W-type hexagonal ferrites, Ceram. Int. 37 (2011) 3691–3696.

[78] F. Leccabue, R. Panizzieri, G. Albanese, G. Leo, N. Suarez Almodovar, Magnetic and mössbauer study of coprecipitated $SrNi_2Fe_{16}O_{27}$ ($SrNi_2W$) and $SrCo_2Fe_{16}O_{27}$ ($SrCo_2W$) hexagonal ferrites, Mater. Res. Bull. 23 (1988) 263–275.

[79] M.L. Mane, R. Sundar, K. Ranganathan, S.M. Oak, K.M. Jadhav, Effects of Nd: YAG laser irradiation on structural and magnetic properties of $Li_{0.5}Fe_{2.5}O_4$, Nucl. Instrum. Methods Phys. Res. Sect. B Beam Interact. Mater. Atoms 269 (2011) 466–471.

[80] J. Xu, G. Ji, H. Zou, Y. Song, S. Gan, Influence of Sm-substitution on structure and electromagnetic properties of $Ba_{3-x}Sm_xCo_2Fe_{24}O_{41}$ powders, J. Magn. Magn. Mater. 323 (2011) 157–162.

[81] J. You, H. Jin Kim, S. Im Yoo, Preparation of strontium W-type hexaferrites in a low oxygen pressure and their magnetic properties, J. Alloy. Comp. 695 (2017) 3011–3017.

[82] C. Singh, S.B. Narang, I. Hudiara, Y. Bai, K. Marina, Hysteresis analysis of Co–Ti substituted M-type Ba–Sr hexagonal ferrite, Mater. Lett. 63 (2009) 1921–1924.

[83] T.M. Clark, B.J. Evans, G.K. Thompson, ^{57}Fe Mössbauer spectroscopic investigation of complex magnetic structures in Ga, Sc, and in substituted M-type hexagonal ferrites, J. Appl. Phys. 85 (1999) 5229.

[84] G. Albanese, A. Deriu, S. Rinaldi, Sublattice magnetization and anisotropy properties of $Ba_3Co_2Fe_{24}O_{41}$ hexagonal ferrite, J. Phys. C Solid State Phys. 9 (1976) 1313–1323.

[85] T. Kikuchi, M. Kobune, M. Nakanishi, T. Fujii, Mössbauer study of zinc-substituted strontium cobalt Z-type hexaferrite, Ceram. Int. 43 (2017) S386–S390.

[86] A.R. Kagdi, N.P. Solanki, F.E. Carvalho, S.S. Meena, P. Bhatt, R.C. Pullar, R.B. Jotania, Influence of Mg substitution on structural, magnetic and dielectric properties of X-type barium-zinc hexaferrites $Ba_2Zn_{2-x}Mg_xFe_{28}O_{46}$, J. Alloy. Comp. 741 (2018) 377–391.

[87] R.A. Nandotaria, R.B. Jotania, C. Singh Sandhu, M. Hashim, S.S. Meena, P. Bhatt, S.E. Shirsath, Magnetic interactions and dielectric dispersion in Mg substituted M-type Sr-Cu hexaferrite nanoparticles prepared using one step solvent free synthesis technique, Ceram. Int. 44 (2018) 4426–4435.

[88] G. Aravind, M. Raghasudha, D. Ravinder, M. Manivel Raja, S.S. Meena, Pramod Bhatt, Mohd Hashim, Study of structural and magnetic properties of Li–Ni nanoferrites synthesized by citrate-gel auto combustion method, Ceram. Int. 42 (2016) 2941–2950.

[89] K. Sharma, S.S. Meena, S. Saxena, S.M. Yusuf, A. Srinivasan, G.P. Kothiyal, Structural and magnetic properties of glass-ceramics containing silver and iron oxide, Mater. Chem. Phys. 133 (2012) 144–150.

[90] K. Sharma, A. Dixit, Sher Singh, Jagannath, S. Bhattacharya, C.L. Prajapat, P.K. Sharma, S.M. Yusuf, A.K. Tyagi, G.P. Kothiyal, Preparation and studies on surface modifications of calcium-silico-phosphate ferrimagnetic glass-ceramics in simulated body fluid, Mater. Sci. Eng. C. 29 (2009) 2226–2233.

[91] K. Sharma, S. Singh, C.L. Prajapat, S. Bhattacharya, Jagannath, M.R. Singh, S.M. Yusuf, G.P. Kothiyal, Preparation and study of magnetic properties of silico phosphate glass and glass-ceramics having iron and zinc oxide, J. Magn. Magn. Mater. 321 (2009) 3821–3828.

[92] K. Sharma, C.L. Prajapat, S.S. Meena, M.R. Singh, S.M. Yusuf, L. Montagne, G.P. Kothiyal, Influence of Au addition on magnetic properties of iron oxide in a silica–phosphate glass matrix, J. Magn. Magn. Mater. 345 (2013) 24–28.

[93] I. Sadiq, S. Naseem, M.N. Ashiq, M.A. Khan, S. Niaz, M.U. Rana, Structural and dielectric properties of doped ferrite nanomaterials suitable for microwave and biomedical applications, Pro Nat Sci-Mater. 25 (2015) 419–424.

[94] H.M. Xiao, X.M. Liu, S.Y. Fu, Synthesis, Magnetic and microwave absorbing properties of core-shell structured $MnFe_2O_4/TiO_2$ nanocomposites, Compos. Sci. Technol. 66 (2006) 2003–2008.

[95] C.C. Chauhana, A.R. Kagdi, R.B. Jotania, A. Upadhyay, C.S. Sandhu, S.E. Shirsath, S.S. Meena, Structural, magnetic and dielectric properties of Co-Zr substituted M-type calcium hexagonal ferrite nanoparticles in the presence of α-Fe_2O_3 phase, Ceram. Int. 44 (2018) 17812–17823.

[96] I. Ali, M.U. Islam, M.S. Awan, M. Ahmad, Effects of heat-treatment time on the structural, dielectric, electrical, and magnetic properties of BaM hexaferrite, J. Mater. Eng. Perform. 22 (2013) 2104–2114.

[97] F.M.M. Pereira, M.R.P. Santos, R.S.T.M. Sohn, J.S. Almeida, A.M.L. Medeiros, M.M. Costa, A.S.B. Sombra, Magnetic and dielectric properties of the M-type barium strontium hexaferrite ($Ba_xSr_{1-x}Fe_{12}O_{19}$) in the RF and microwave (MW) frequency range, J. Mater. Sci. Mater. Electron. 20 (2009) 408–417.

[98] J. Chand, M. Singh, Electric and dielectric properties of $MgGd_{0.1}Fe_{1.9}O_4$ ferrite, J. Alloy. Comp. 486 (2009) 376.

[99] R. Sharma, P. Pahuja, R.P. Tandon, Structural, dielectric,ferromagnetic, ferroelectric and ac conductivity studies of the $BaTiO_3$–$CoFe_{1.8}Zn_{0.2}O_4$ multiferroic particulate composites, Ceram. Int. 40 (2014) 9027–9036.

[100] J.C. Maxwell, Electricity and Magnetism, Oxford University Press, London, 1973.

[101] H. Yang, H. Wang, L. He, L. Shui, X. Yao, Polarization relaxation mechanism of $Ba_{0.6}Sr_{0.4}TiO_3/Ni_{0.8}Zn_{0.2}Fe_2O_4$ composite with giant dielectric constant and high permeability, J. Appl. Phys. 108 (1–6) (2010), 074105.

[102] P.V. Reddy, T.S. Rao, Dielectric behaviour of mixed Li-Ni ferrites at low frequencies, J. Less Common. Met. 86 (1982) 255–261.

[103] Ashima, S. Sanghia, A. Agarwal, Reetu, N. Ahlawat, J. Monica, Appl. Phys. 112 (1–8) (2012), 014110.

[104] I. Sadiq, E.V. Rebrov, S. Naseem, M. NaeemAshiq, M.U. Rana, Influence of Nd-Co substitution on structural, electrical, and dielectric properties of X-type hexagonal nanoferrites, J. Mater. Eng. Perform. 23 (2014) 622–627.

[105] S. Dutta, R.N.P. Choudhry, P.K. Sinha, Impedance spectroscopy studies on Gaion- PLZT ceramics, Phys. Status Solidi A 202 (2005) 1172–1181.

[106] M.N. Ashiq, M.J. Iqbal, I.H. Gul, Structural, electrical and magnetic properties of Zr-Cd substituted strontium hexaferrite ($SrFe_{12}O_{19}$) nanoparticles, J. Alloy. Comp. 487 (2009) 341–345.

[107] V.R.K. Murthy, J. Sobhanadri, Dielectric properties of some nickel-zinc ferrites at radio frequency, Phys. Status Solidi A 36 (1976) K133–K135.

[108] O. Prakash, K.D. Mandal, C.C. Chistopher, Electronic Processes in Ionic Crystals, Oxford Univ. Press, London, 1948.

[109] D. Alder, J. Feienleib, Electrical and optical properties of narrow-band materials, Phys. Rev. B 2 (1970) 3112–3134.

[110] S.L. Kadam, C.M. Kanamadi, K.K. Patankar, B.K. Chougule, Dielectric behaviour and magnetoelectric effect in $Ni_{0.5}Co_{0.5}Fe_2O_4$+$Ba_{0.8}Pb_{0.2}TiO_3$ ME composites, Mater. Lett. 59 (2005) 215–219.

[111] M.Y. Lodhia, M.A. Khana, M.N. Akhtar, M.F. Warsi, A. Mahmood, S.M. Ramay, Role of Nd-Ni on structural, spectral and dielectric properties of strontium barium based nano-sized X-type ferrites, Ceram. Int. 44 (2018) 2968–2975.

[112] J.R. Macdonald, Impedance Spectroscopy: Emphasizing Solid State Material and Systems, Wiley, New York, 1987.

[113] M. Kaiser, Electrical conductivity and complex electric modulus of titanium doped nickel–zinc ferrites, Physica B 407 (2012) 606–613.

[114] A. Mishra, S.N. Choudhary, K. Prasad, R.N.P. Choudhary, Complex impedance spectroscopic studies of $Ba(Pr_{1/2}Ta_{1/2})O_3$ceramic, Physica B 406 (2011) 3279–3284.

[115] K.P. Padmasree, D.K. Kanchan, A.R. Kulkarni, Impedance and modulus studies of the solid electrolyte system 20CdI2 -80 [$xAg_{2O\text{-}y}(0.7V_2\ O_5\text{-}0.3B_2O_3)$], where $1 \leq x/y \leq 3$, Solid State Ion. 177 (2006) 475–482.

[116] M. Irfan, A. Elahi, A. Shakoor, Hysteresis and Electric modulus analysis of Y^{3+} doped MnNi –Y –type hexagonal ferrite, Ceramics 60 (2016) 34–40.

[117] S.M. Patange, S.E. Shirsath, K.S. Lohar, S.S. Jadhav, N. Kulkarni, K.M. Jadhav, Electrical and switching properties of $NiAl_xFe_{2-x}O_4$ ferrites synthesized by a chemical method, Physica B 406 (3) (2011) 663–668.

[118] A. Bagum, M.B. Hossen, F.U.Z. Chowdhury, Complex impedance and electric modulus studies of Al substituted $Co_{0.4}Cu_{0.2}Zn_{0.4}Al_xFe_{2-x}O_4$ ferrites prepared by auto combustion technique, Ferroelectrics 494 (2016) 19–32.

[119] M.M. Costa, G.F.M. Pires Junior, A.S.B. Sombra, Dielectric and impedance properties studies of the of lead doped (PbO)-Co_2Y type hexaferrite

$Ba_2Co_2Fe_{12}O_{22}(Co_2Y)$), Mater. Chem. Phys. 123 (2010) 35–39.
[120] M. Raghasudha, D. Ravinder, P. Veerasomaiah, S. goud, G.S. Goud, B. Rambabu, N. Venkatesh, Impedance studies on chromium substituted cobalt nanoferrites, Int. J. Nanosci. Nanotechnol. 1 (2015) 6–7.
[121] E. Pervaiz, I.H. Gul, Influence of rare earth (Gd^{3+}) on structural, gigahertz dielectric and magnetic studies of cobalt ferrite, J. Phys. Conf. Ser. 439 (1–15) (2013), 012015.
[122] Y. Bai, J. Zhou, Z. Gui, L. Li, Electrical properties of non-stoichiometric Y-type hexagonal ferrite, J. Magn. Magn. Mater. 278 (1) (2004) 208–213.
[123] M.G. Chourashiya, J.Y. Patil, S.H. Pawar, L.D. Jadhav, Studies on structural, morphological and electrical properties of $Ce_{1-x}Gd_xO_{2-(x/2)}$, Mater. Chem. Phys. 109 (1) (2008) 39–44.
[124] M.T. Farid, I. Ahmad, M. Kanwal, G. Murtaza, I. Ali, S.A. Khan, The role of praseodymium substituted ions on electrical and magnetic properties of Mg spinel ferrites, J. Magn. Magn. Mater. 428 (2017) 136–143.
[125] H. Sözeri, H. Deligöz, H. Kavas, A. Baykal, Magnetic, dielectric and microwave properties of M–Ti substituted barium hexaferrites (M = Mn^{2+}, Co^{2+}, Cu^{2+},Ni^{2+}, Zn^{2+}), Ceram. Int. 40 (2014) 8645–8657.
[126] Z. Zhang, X. Liu, X. Wang, Y. Wu, R. Li, Effect of Nd–Co substitution on magnetic and microwave absorption properties of $SrFe_{12}O_{19}$ hexaferrites, J. Alloy. Comp. 525 (2012) 114–119.
[127] S. Gairola, V. Verma, A. Singh, L. Purohit, R. Kotnala, Modified composition of barium ferrite to act as a microwave absorber in X-band frequencies, Solid State Commun. 150 (2010) 147–151.